

# Competing retention pathways of uranium upon reaction with Fe(II)

Michael S. Massey<sup>a,\*</sup>, Juan S. Lezama-Pacheco<sup>a</sup>, Morris E. Jones<sup>a</sup>,  
Eugene S. Ilton<sup>b</sup>, José M. Cerrato<sup>c,1</sup>, John R. Bargar<sup>d</sup>, Scott Fendorf<sup>a,\*</sup>

<sup>a</sup> Department of Environmental Earth System Science, Stanford University, Stanford, CA 94305, United States

<sup>b</sup> Pacific Northwest National Laboratory, Richland, WA 99352, United States

<sup>c</sup> Department of Energy, Environmental, and Chemical Engineering, Washington University in Saint Louis, One Brookings Drive, Saint Louis, MO 63130, United States

<sup>d</sup> SLAC National Accelerator Laboratory, 2575 Sand Hill Road, Menlo Park, CA 94025, United States

Received 23 August 2013; accepted in revised form 15 July 2014; available online 29 July 2014

## Abstract

Biogeochemical retention processes, including adsorption, reductive precipitation, and incorporation into host minerals, are important in contaminant transport, remediation, and geologic deposition of uranium. Recent work has shown that U can become incorporated into iron (hydr)oxide minerals, with a key pathway arising from Fe(II)-induced transformation of ferrihydrite,  $(\text{Fe}(\text{OH})_3 \cdot n\text{H}_2\text{O})$  to goethite ( $\alpha\text{-FeO}(\text{OH})$ ); this is a possible U retention mechanism in soils and sediments. Several key questions, however, remain unanswered regarding U incorporation into iron (hydr)oxides and this pathway's contribution to U retention, including: (i) the competitiveness of U incorporation versus reduction to U(IV) and subsequent precipitation of  $\text{UO}_2$ ; (ii) the oxidation state of incorporated U; (iii) the effects of uranyl aqueous speciation on U incorporation; and, (iv) the mechanism of U incorporation. Here we use a series of batch reactions conducted at pH  $\sim 7$ ,  $[\text{U(VI)}]$  from 1 to 170  $\mu\text{M}$ ,  $[\text{Fe(II)}]$  from 0 to 3 mM, and  $[\text{Ca}]$  at 0 or 4 mM coupled with spectroscopic examination of reaction products of Fe(II)-induced ferrihydrite transformation to address these outstanding questions. Uranium retention pathways were identified and quantified using extended X-ray absorption fine structure (EXAFS) spectroscopy, X-ray powder diffraction, X-ray photoelectron spectroscopy, and transmission electron microscopy. Analysis of EXAFS spectra showed that 14–89% of total U was incorporated into goethite, upon reaction with Fe(II) and ferrihydrite. Uranium incorporation was a particularly dominant retention pathway at U concentrations  $\leq 50 \mu\text{M}$  when either uranyl–carbonate or calcium–uranyl–carbonate complexes were dominant, accounting for 64–89% of total U. With increasing U(VI) and Fe(II) concentrations, U(VI) reduction to U(IV) became more prevalent, but U incorporation remained a functioning retention pathway. These findings highlight the potential importance of U(V) incorporation within iron oxides as a retention process of U across a wide range of biogeochemical environments and the sensitivity of uranium retention processes to operative (bio)geochemical conditions. © 2014 Elsevier Ltd. All rights reserved.

\* Corresponding authors. Present address: Department of Earth and Environmental Sciences, California State University East Bay, 25800 Carlos Bee Boulevard, Hayward, CA 94542, United States. Tel.: +1 (510)885 3486 (M.S. Massey).

E-mail address: [mike.massey@csueastbay.edu](mailto:mike.massey@csueastbay.edu) (M.S. Massey).

<sup>1</sup> Present address: Department of Civil Engineering, University of New Mexico, 210 University Boulevard NE, Albuquerque, NM 87131, United States.

## 1. INTRODUCTION

Uranium mining, milling, refining, and nuclear weapons production in the United States has left a legacy of soil and groundwater contamination at a variety of sites such as Hanford, WA and Oak Ridge, TN. The United States Department of Energy manages an inventory of

1.5 billion m<sup>3</sup> of contaminated groundwater, and 75 million m<sup>3</sup> of contaminated soil/sediment (DOE, 1997); U is among the most common radionuclide contaminants at DOE sites (Riley and Zachara, 1992). Uranium contamination from legacy U production exists on every continent except Antarctica, with an estimated global volume of over 900 million m<sup>3</sup> of tailings, covering nearly 6000 ha, with associated contamination of soils, sediments, and groundwater (IAEA, 2004). Managing this legacy U contamination requires an accurate understanding of U biogeochemical processes and sequestration mechanisms. Uranium biogeochemistry also plays key roles in U extraction/mining, U contamination remediation, and environmental fate and transport of U. Thus, establishing a clearer understanding of U biogeochemistry is crucial for mitigating the impact of legacy contamination, as well as understanding current and future environmental impacts of U.

In the subsurface environment, U retention processes remove U from the groundwater in which it is transported, concentrating it in potentially economically extractable quantities (e.g., in roll-front deposits), and alleviating U toxicity risks in groundwater. Uranium sequestration mechanisms are heavily influenced by U oxidation state: U(VI) is the most mobile form in the environment and exists as the uranyl cation,  $\text{UO}_2^{2+}$ , and associated species, while U(IV) tends to form sparingly-soluble precipitates such as uraninite ( $\text{UO}_2(\text{s})$ ). Recent theoretical studies (Skomurski et al., 2011; Wander and Shuford, 2012) and laboratory work (Ilton et al., 2005, 2010, 2012) suggest that U(V) might also be environmentally relevant. However, field-based evidence for U(V) is rare, with only one U(V) mineral (wyartite), having been identified (Burns and Finch, 1999). There are four primary U retention pathways: adsorption of U(VI), precipitation of U(VI) minerals such as uranyl silicates (Catalano and Brown, 2004; Burns, 2005) or phosphates (Stubbs et al., 2009), reductive precipitation of U(IV) (Lovley and Phillips, 1992b; Liger et al., 1999; Du et al., 2011; Latta et al., 2012b), and, incorporation/co-precipitation of U in host minerals such as iron oxides (collectively used here to refer to hydroxides, oxyhydroxides, and oxides) (Payne et al., 1994; Duff et al., 2002; Nico et al., 2009; Stewart et al., 2009; Ilton et al., 2010, 2012; Boland et al., 2011; Marshall et al., 2014), or silicates (Allard et al., 1999; Soderholm et al., 2008).

Uranyl adsorption is dependent on pH, U aqueous speciation, and mineralogical constituents. Waite et al. (1994) found nearly complete uranyl adsorption on ferrihydrite at circumneutral pH. Aqueous uranyl-carbonate and uranyl-calcium-carbonate ternary complexes also decrease the extent of U adsorption (Stewart et al., 2010). However, adsorption does occur in the presence of uranyl-carbonate and uranyl-calcium-carbonate complexes as an inner-sphere uranyl-carbonate (Bargar et al., 1999) or uranyl surface complex (Hiemstra et al., 2009; Rossberg et al., 2009). Uranium adsorption is fast but ultimately reversible, thus operating as a primarily short-term retention mechanism.

Uranium in the hexavalent oxidation state also forms minerals such as uranyl hydroxides (e.g., schoepite and metaschoepite), uranyl silicates (e.g., uranophane), uranyl

carbonates (e.g., liebigite), and uranyl phosphates (e.g., autunite, torbernite and metatorbernite) (Finch and Murakami, 1999; Burns, 2005). Uranyl minerals are a potential sink for U and have been found at contaminated sites (Catalano et al., 2004; Wang et al., 2005; Stubbs et al., 2009). Precipitation of uranyl minerals may be important for U retention in oxygenated environments such as arid or semi-arid soils and sediments, if the minerals limit U migration and mitigate toxic impacts.

Reductive precipitation of U as U(IV) has also been extensively studied, chiefly as an *in situ* remediation technique (Lovley and Phillips, 1992b; Anderson et al., 2003; Wu et al., 2006; Neiss et al., 2007; Yabusaki et al., 2007). Uranium is retained as sparingly-soluble uraninite (e.g., Suzuki et al., 2002), or as “monomeric” or “mononuclear” U(IV) (e.g., Bernier-Latmani et al., 2010; Boyanov et al., 2011). Uranium reduction can occur via biotic or abiotic processes. Abiotically, U reduction is facilitated by reaction with Fe(II), which can be catalyzed by mineral surfaces (Liger et al., 1999; Chakraborty et al., 2010; Latta et al., 2012a). Heterogeneous U reduction by reduced minerals such as Fe sulfides and magnetite is also possible (Hua and Deng, 2008; Latta et al., 2012b; Hyun et al., 2012; Singer et al., 2012), as is homogeneous U reduction by aqueous Fe(II) (Du et al., 2011) or sulfide (Hua et al., 2006). Biotically, various dissimilatory metal reducing bacteria can use U for respiration (Lovley and Phillips, 1992b; Wilkins et al., 2006), while others reduce U via a non-respiratory pathway (Lovley and Phillips, 1992a). However, the rate and extent of U reduction is diminished by uranyl-calcium-carbonate complexes (Brooks et al., 2003; Boyanov et al., 2007; Neiss et al., 2007; Sheng et al., 2011; Singer et al., 2012), with inhibition occurring due to kinetic rather than thermodynamic factors (Stewart et al., 2007).

Uranium may also be retained through incorporation within the structure of other host minerals. For example, Pett-Ridge et al. (2007) concluded that non-exchangeable U in 150–4100 ka Hawaiian soils was co-precipitated with Fe to form iron oxides, and Sato et al. (1997) showed that iron oxides scavenged greater than 8% U (by weight) from waters down gradient of the Koongarra deposit in Australia. Because of a spatial correlation among U, Cu, and P, Sato et al. (1997) postulated that U was present in both a torbernite/metatorbernite ( $\text{Cu}(\text{UO}_2)_2(\text{PO}_4)_2 \cdot 8\text{--}12\text{H}_2\text{O}$ ) phase and a goethite phase. Payne and Airey, 2006 postulated an adsorption step followed by solid phase incorporation during mineral ripening to more crystalline phases.

While the above examples demonstrate the importance of co-precipitation on geologic time scales, this process is also active on much shorter time scales of days to decades. For example, at the United States Department of Energy's Oak Ridge site, Stubbs et al. (2006) identified not only distinct uranyl phosphate phases but also goethite-associated U as phases controlling the aqueous concentration of U. In addition, Gómez et al., 2006 concluded that U co-precipitation with iron oxides controlled the release of U from an abandoned U mine in Spain. Senko et al. (2005) also noted that addition of Fe(II) during oxidation of authigenic  $\text{UO}_2$ -bearing solids resulted in diminished release of aqueous U(VI), which is consistent with U(VI/V) incorporation into

transforming/precipitating Fe(III) oxides. Gu et al. (2003) also postulated, on the basis of uptake and extraction data, that U co-precipitation with Fe and/or Al oxides had a significant influence on dissolved concentrations of U.

Uranium incorporation has been demonstrated in hematite (Duff et al., 2002; Ilton et al., 2012; Marshall et al., 2014) after heating and aging of U and Fe co-precipitates. Payne et al. (1994) also found that U adsorbed on ferrihydrite became resistant to extraction after heating and aging transformed the ferrihydrite to hematite and lesser amounts of goethite. Uranium incorporation into octahedral Fe(III) sites in goethite has been posited (Nico et al., 2009; Boland et al., 2011), and U incorporation into magnetite has also been proposed (Nico et al., 2009). In all experiments, U that had purportedly incorporated into iron oxides was resistant to extraction and re-mobilization (Duff et al., 2002; Smith et al., 2009; Stewart et al., 2009; Ilton et al., 2012). Whether by heating or Fe(II)-induced transformation, the incorporation of U into iron oxides can occur in days to weeks (Nico et al., 2009; Boland et al., 2011). Iron(II)-induced transformation of ferrihydrite to goethite occurs as a coupled dissolution–reprecipitation process (Hansel et al., 2003) and U is incorporated into the goethite lattice during the transformation. Since U incorporation can result in U that is resistant to re-mobilization (Stewart et al., 2009), U incorporation into transforming iron oxides can strongly retain U, potentially over long periods of time.

Kerisit et al. (2011) conducted atomistic modeling of U incorporated in the structure of various iron oxides. The simulated local structures around U(V) or U(VI) in Fe(III) sites yielded a good match with the EXAFS data reported by Nico et al. (2009). Charge balance was maintained by protonation/de-protonation of neighboring hydroxyl groups and/or the introduction of vacancies at other Fe(III) sites. The combination of modeling and experimental approaches provide strong evidence for U(V/VI) incorporation into the structure of goethite during reductive transformation of ferrihydrite. However, important aspects of the U incorporation mechanism and resulting solid-phase product(s) remain unresolved. The objective of the present work was therefore to address several knowledge gaps, including: (1) the relevance of U incorporation at commonly-observed concentrations of calcium, carbonate, U, and Fe; (2) the mechanisms by which U is incorporated, including the valence state of incorporated U; and, (3) competition between U incorporation, reduction, and adsorption processes.

## 2. METHODS

### 2.1. Sample preparation and solution chemical analyses

#### 2.1.1. Two-line ferrihydrite preparation

Two-line ferrihydrite slurry was prepared according to the method outlined in Herbel and Fendorf (2006). Briefly, ~150 mM ferric chloride was vigorously mixed using a mechanical stirrer, and rapidly (within ~15 min) titrated to a pH of 7.0–7.5 using 0.4–1 M sodium hydroxide. After 1–2 h of equilibration and further addition of sodium hydroxide to establish a stable pH in the 7.0–7.5 range,

the slurry was allowed to settle, and the supernatant was decanted. The slurry was then centrifuged and washed with de-ionized water (18 M $\Omega$ ) five times to remove residual salts. Two-line ferrihydrite mineralogy was confirmed using high-resolution synchrotron X-ray powder diffraction at beamline 7-2 at the Stanford Synchrotron Radiation Lightsource (SSRL). Slurry density was measured by the ferrozine assay (Stookey, 1970) following dissolution of ferrihydrite in 6 M hydrochloric acid and complete reduction of Fe(III) to Fe(II) using 0.5 M hydroxylamine hydrochloride.

In order to compare the present study with previous experiments (e.g., Nico et al., 2009), ferrihydrite-coated sand was also prepared using the method described by Brooks et al. (1996). Ferrihydrite slurry was prepared as above, and mixed with pure quartz sand (Unimin Corporation, New Canaan, Connecticut, United States).

#### 2.1.2. Variable U(VI) incubations

Ferrihydrite slurry was incubated with 300  $\mu$ M Fe(II) and 1–170  $\mu$ M uranyl to determine the distribution of U retention pathways across a range of initial U(VI) concentrations. Batch incubations were performed in 125 mL glass serum vials with thick rubber septum stoppers (Bellco Glass, Inc., New Jersey, United States). Two sample series were prepared: a no-Ca series, and a series with 4 mM Ca. A solution with a final concentrations of 10 mM piperazine-N,N'-bis(2-ethansulfonic acid) (PIPES) buffer, 3.8 mM KHCO<sub>3</sub>, and 0 or 4 mM CaCl<sub>2</sub>, adjusted to pH 7.0, served as the aqueous reaction medium. Ferrihydrite slurry ( $1.7 \times 10^{-4}$  mol Fe bottle<sup>-1</sup>) and varying concentrations of uranyl acetate (0, 1, 3, 5, 10, 50, 100, 170  $\mu$ M) were added to each reaction vessel. Ferrihydrite-coated sand samples were prepared with 1 g of ferrihydrite-coated sand (also approximately  $1.7 \times 10^{-4}$  mol Fe bottle<sup>-1</sup>, as in the slurry experiments) rather than ferrihydrite slurry. The ferrihydrite-coated sand experiment used the same aqueous reaction medium, with 4 mM Ca, and 170  $\mu$ M U. Then the mixture in each vessel was allowed to equilibrate for ~1 h, and spiked with 300  $\mu$ M Fe(II) (added as FeSO<sub>4</sub>). The total solution volume in all cases was 100 mL. A no-Fe(II), no-Ca, 50  $\mu$ M U sample was also made as a standard for uranyl adsorption on ferrihydrite. An incubation where 50  $\mu$ M U was added after ferrihydrite transformation was also performed, to evaluate the ability for U to be incorporated into goethite after transformation. The entire procedure was performed using de-oxygenated, de-ionized (18 M $\Omega$ ) water in an anoxic (95% N<sub>2</sub>, 5% H<sub>2</sub>) atmosphere (Coy Laboratory Products Inc., Michigan, United States).

Samples were incubated outside of the anaerobic glovebag at 25 °C for 8–10 days on a rotary shaker at 120 RPM. After incubation, 10 mL aliquots of solution were withdrawn using a syringe, and filtered through 0.22  $\mu$ m membranes into 25 mL serum vials. Serum vials were then capped with rubber septum stoppers and stored at 4 °C until analysis. The remaining solution/slurry mixture was vacuum filtered onto a 0.22  $\mu$ m pore membrane filter (Millipore, Inc., Massachusetts, United States) and rinsed with de-ionized water. While still wet, samples were scraped from the filters and allowed to dry prior to grinding and

analysis. All sample harvesting and processing was performed in an anoxic atmosphere, as above. This process yielded ~15–20 mg of dried iron oxide powder per 125 mL serum vial. Between 3–6 replicates of each incubation were performed in separate bottles, and combined to ensure sufficient mass of sample for analysis. Iron-coated sand samples were not ground and were simply dried for analysis.

#### 2.1.3. Variable Fe(II) incubations

Constant-U, variable-Fe(II) incubations were also performed to evaluate the effect of Fe(II) on U incorporation and U reduction to U(IV). As in the variable-U incubations described above, the solutions had a final reaction volume of 100 mL per 125 mL serum bottle, and all incubations were conducted in an anoxic atmosphere. The solutions consisted of 10 mM PIPES buffer, 3.8 mM sodium bicarbonate, either 0 or 4 mM  $\text{CaCl}_2$ , and 127  $\mu\text{M}$  uranyl acetate. Two-line ferrihydrite slurry was added to a final density of  $1.7 \times 10^{-4}$  mol Fe bottle<sup>-1</sup>. Bottles were sealed and allowed to equilibrate for ~1 h, after which Fe(II) was added by syringe to concentrations ranging from 0 to 3 mM (0, 0.3, 1, and 3 mL of 100 mM  $\text{FeSO}_4$ ). Bottles were shaken at 120 RPM at 25 °C for 10 days outside of the anaerobic chamber.

After 10 days the bottles were returned to the anaerobic chamber for sampling. A 0.5 mL sample of well-mixed slurry was dissolved in 1 mL of 3 M HCl for total Fe analysis. The remaining slurry was vacuum filtered through nylon filters with 0.22  $\mu\text{m}$  pores. Aliquots of 0.5 mL of the filtrate were dissolved in 1 mL of 3 M HCl for solution Fe analysis. Aliquots for total dissolved metal analysis were prepared by acidifying 22 mL of the filtrate to a final concentration of 2%  $\text{HNO}_3$  (22 mL filtrate and 500  $\mu\text{L}$  ~70%  $\text{HNO}_3$ ). The remaining filtrate was sealed in 22 mL tubes with no headspace for dissolved inorganic carbon and pH analysis. Solids were rinsed in 10 mL de-ionized water for 24 h, then dried under anoxic conditions, and finally, ground into powder for analysis.

#### 2.1.4. Bicarbonate extraction

Several samples from the variable U, no-Ca series (1, 5, and 10  $\mu\text{M}$  U), and one sample from the Ca series (3  $\mu\text{M}$  U) were subjected to a 30 mM  $\text{KHCO}_3$  extraction to remove and quantify adsorbed U. Bicarbonate extraction of adsorbed uranyl also clarified (via removal of adsorbed species) the X-ray absorption spectrum of non-adsorbed, solid-phase U in these samples. Samples for extraction were harvested as in Section 2.1.2 above, but rather than being dried, they were placed in a separate serum vial with 20 mL of bicarbonate extractant (per bottle of solid sample) and shaken for an additional 4 days at 120 RPM. Aliquots of 10 mL of extractant solution were then taken with a syringe and filtered for ICP-MS analysis in a matrix of 2%  $\text{HNO}_3$ , and the remaining extractant/slurry mixture was vacuum filtered, washed, scraped, dried, and ground into powder for analysis, as in Sections 2.1.2 and 2.1.3, above.

Replicate samples from the variable Fe(II) series were also subjected to a 15 mM sodium bicarbonate extraction to quantify adsorbed U. After bicarbonate extraction,

solids were filtered on 0.22  $\mu\text{m}$  nylon filters, and the extractant solution was preserved in 2%  $\text{HNO}_3$  for U analysis by ICP-MS. Solids were rinsed using 10 mL of de-ionized water, dried under anoxic conditions, and ground for analysis.

#### 2.1.5. Solution analysis

Aliquots of reaction medium and extractant solution were analyzed for U using ICP-MS (Thermo Scientific XSERIES 2, Thermo Fisher Scientific, Waltham, MA), and Ca, K, Fe, Na, and Si using ICP-OES (Thermo Scientific ICAP 6300 Dual View, Thermo Fisher Scientific, Waltham, MA). Samples were diluted in a matrix of ~2% trace-metal grade nitric acid prior to analysis.

### 2.2. Solid phase analyses

#### 2.2.1. Ascorbic acid extraction/dissolution experiments

Quantities of ~10 mg of U-containing iron oxide samples (10 and 100  $\mu\text{M}$  U, 0 and 4 mM Ca) were dissolved in 50 mL of 10 mM ascorbic acid at pH ~3 in an anoxic atmosphere. The method used was similar to previous studies (Postma, 1993; Larsen and Postma, 2001; Boland et al., 2011). Samples of 1 mL were taken at 1, 15, 30, 60, 240, and 480 min, as well as 1, 2, 4, 6, 12, and 18 days. After 18 days, any remaining solids were completely dissolved by adding 8 mL of concentrated nitric acid (67–70%  $\text{HNO}_3$  by mass) and 2 mL of concentrated hydrochloric acid (34–37% HCl by mass), in order to obtain total U and Fe. All solution aliquots were filtered through syringe filters with 0.22  $\mu\text{m}$  pores, diluted with de-ionized water, and analyzed via ICP-MS for U, Fe, and Ca.

#### 2.2.2. X-ray absorption spectroscopy

A quantity of ~15 mg of dried iron oxide powder was combined with ~70 mg boron nitride powder under oxygen-free conditions, and homogenized by repeated grinding before being pressed into pellets for EXAFS analysis in aluminum sample holders with a double layer of Kapton film. The primary sample holders were then placed into secondary indium-sealed holders with Kapton windows to provide further sample containment and isolation from oxygen during analysis. Ferrihydrite-coated sand samples were not mixed with boron nitride. All samples were analyzed at beamlines 11-2 and 4-1 at SSRL. Data collection was performed at room temperature, under vacuum (~ $10^{-6}$  torr) to isolate the samples from oxygen and thereby prevent oxidation. The X-ray beam incident energy was controlled via a Si(220) double-crystal monochromator in the  $\phi = 0^\circ$  orientation, detuned ~30% at 17.6 keV to eliminate higher-order harmonics. Transmission spectra were collected using an in-line ionization chamber, and fluorescence spectra were collected simultaneously using either a 13- or 30-element Ge solid-state detector (Canberra, Connecticut, United States), or a Lytle detector. An in-line Y foil was used to ensure energy calibration; the inflection point in the Y K-edge spectrum (defined using the first-derivative peak) was calibrated to 17038.4 eV. Data calibration and averaging were performed using SixPack (Webb, 2005), and data were normalized, background-subtracted, and fit using the

Athena and Artemis software packages (Ravel, 2001; Ravel and Newville, 2005) and FEFF 6 or FEFF 8.4 (Ankudinov et al., 1998). Detailed normalization and fitting parameters are provided in the [Electronic Annex](#).

### 2.2.3. X-ray powder diffraction

For X-ray powder diffraction (XRD) analysis, finely ground iron oxide powder was placed into 0.3 mm diameter borosilicate glass capillaries. Capillaries were flame-sealed on one end, sealed with five-minute Epoxy (ITW Devcon, Danvers, MA) on the other end, and analyzed at beamline 7-2 at SSRL. Capillaries were contained in sealed polycarbonate containers with Kapton windows. The container was also purged with He gas to prevent exposure to oxygen and decrease the scattering background. The incident beam energy was maintained at 16.5 keV ( $\lambda = 0.75 \text{ \AA}$ ); precise energy and diffractometer calibration was achieved using a LaB<sub>6</sub> calibration standard in a borosilicate glass capillary. Powder diffraction data were collected over a Q-space range of 0.8 to  $\sim 10\text{--}12 \text{ \AA}^{-1}$  using a single-channel energy dispersive Vortex solid-state detector.

Diffraction patterns were analyzed using the General Structure Analysis System (GSAS) software package (Larson and Von Dreele, 2000) with the EXPGUI interface (Toby, 2001). Peaks were assigned to goethite, magnetite, and UO<sub>2</sub> using molecular models of those minerals.

### 2.2.4. Transmission electron microscopy

Dried, ground samples of the 10 and 100  $\mu\text{M}$  U/iron oxide suspensions (4 mM Ca, prepared as in Section 2.1.2) were suspended in ethanol and applied to carbon support grids (Ted Pella, Inc., Redding, California, United States) for examination via transmission electron microscopy (TEM) and energy-dispersive X-ray spectroscopy (EDS). Preparation of TEM grids was carried out in an anoxic atmosphere (95% N<sub>2</sub>, 5% H<sub>2</sub>), and samples were stored and transported in an anoxic atmosphere until transfer to the TEM vacuum chamber. Samples were analyzed at the Stanford Nanocharacterization Laboratory using a FEI Tecnai G2 F20 X-TWIN Transmission Electron Microscope (FEI, Hillsboro, Oregon, United States). The field emission gun TEM was operated at an accelerating voltage of 200 kV, and images were collected using a CCD camera.

### 2.2.5. X-ray photoelectron spectroscopy

Samples of 10 and 100  $\mu\text{M}$  U/iron oxide suspensions prepared as in Section 2.1.2 (both 4 mM Ca and no-Ca systems, with 0.3 mM Fe(II)) were filtered, rinsed with de-gassed DI water, dried, fixed on indium coupons, and transferred into the analysis chamber through an anoxic glovebox attached to the instrument for X-ray photoelectron spectroscopic (XPS) analysis. The samples were analyzed using a Kratos Axis Ultra DLD spectrometer at room temperature. The instrument was operated at an excitation voltage of 15 kV with a 10 mA current, using monochromatic Al K $\alpha$  X-rays (1486.7 eV). A pass energy of 20 or 40 eV, with a step size of 0.1 or 0.125 eV, enabled high-resolution analysis, with high collection efficiencies achieved using a magnetic immersion lens. Binding energies were referenced to the adventitious C1s peak at 285.0 eV.

The primary and satellite peaks for U4f were used in the fitting procedure following the methodology outlined in Ilton et al. (2010) and Ilton and Bagus (2011). High-resolution U4f regional spectra, spanning a spectral region from 375 to 405 eV, were best fit after Shirley background subtractions by nonlinear least-squares using the CasaXPS curve resolution software, with parameters similar to those in Ilton et al. (2010).

## 3. RESULTS

### 3.1. Variable U incubations

Variable concentrations (1–170  $\mu\text{M}$  U) of uranyl were reacted with ferrihydrite and 300  $\mu\text{M}$  Fe(II) at pH 7.0, with 0 or 4 mM Ca; Fe(II) was used to drive the reductive transformation of both ferrihydrite and U. In the absence of Ca, near complete sorption of U occurred at initial aqueous concentrations below 10  $\mu\text{M}$ ; the amount of U remaining in solution was  $\leq 0.01 \mu\text{M}$  (Fig. 1). The presence of calcium increased the aqueous phase concentration ten-fold, owing to the stability of the aqueous uranyl–calcium–carbonate ternary complex. However, greater than 95% of the initial U was retained on (or in) the solid phase at initial U concentrations of 1–10  $\mu\text{M}$  (Fig. 1). Uranium retention remained greater than 90% of the initial U added at  $[\text{U(VI)}]_{\text{initial}} < 170 \mu\text{M}$  in the absence of Ca, but when Ca was present at a concentration of 4 mM less than 40% of an initial 170  $\mu\text{M}$  U was retained (Fig. 1).

When solids resulting from the systems with  $[\text{U(VI)}]_{\text{initial}} = 10$  and 100  $\mu\text{M}$  were reacted with 10 mM ascorbic acid at pH  $\sim 3.0$ , approximately 20–40% of solid-phase U was removed from the solid within 1 h of reaction; Fe dissolution was not observed during this reaction period (Fig. 2). The release of U during the initial 1 h period is attributed to desorption of uranyl from the iron oxide surface. Iron oxide dissolution was slow, as was further U release, with 58–83% of both total Fe and total U being released from the solid phase after 18 d of reaction with ascorbic acid (Fig. 2). On the basis of the ascorbic acid extraction, it appears that less than 40% of the U was retained on the iron oxide surface, with the remainder occluded within the Fe solid. Further, the U within the iron oxides underwent retarded release upon reaction with ascorbic acid due to the slow dissolution rate of the host minerals.

#### 3.1.1. Uranium solid phase speciation

Uranium solid-phase speciation was investigated using EXAFS spectroscopy and linear combination fitting. On the basis of U axial oxygen coordination, approximately 15% of the “incorporated” reference spectrum (after bicarbonate extraction) was an un-extracted uranyl species, either adsorbed or otherwise occluded in the iron oxide (Fig. 3), while the remainder (85%) was U in octahedral (uranate) coordination. Adsorbed and “nano”-UO<sub>2</sub> compounds used for linear combination fitting reference spectra were entirely adsorbed uranyl or UO<sub>2</sub> (see [Electronic Annex](#) for fitting details). Linear combination fits (details of which are provided in [Electronic Annex](#)) were adequate

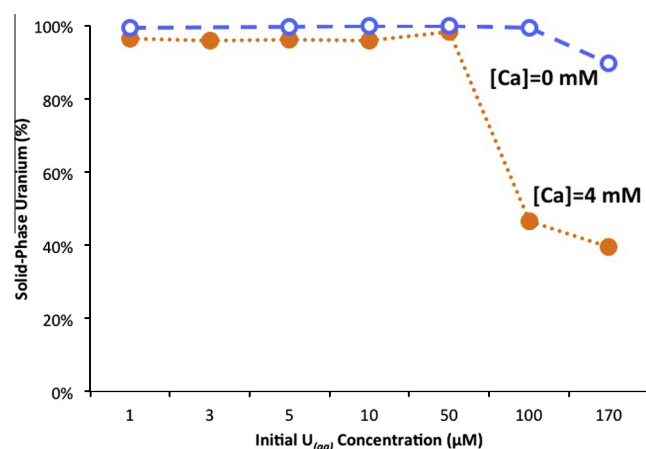


Fig. 1. Uranium partitioned into the solid phase as a function of  $U(VI)_{(aq)}$  concentration ( $[U]_{initial} = 1\text{--}170\text{ }\mu\text{M}$ ) and  $Ca^{2+}_{(aq)}$  concentration (0 or 4 mM Ca) upon reaction with ferrihydrite, 0.3 mM Fe(II), and 3.8 mM carbonate at a pH of 7.0. Error bars are smaller than the symbols used to represent the data and are not displayed.

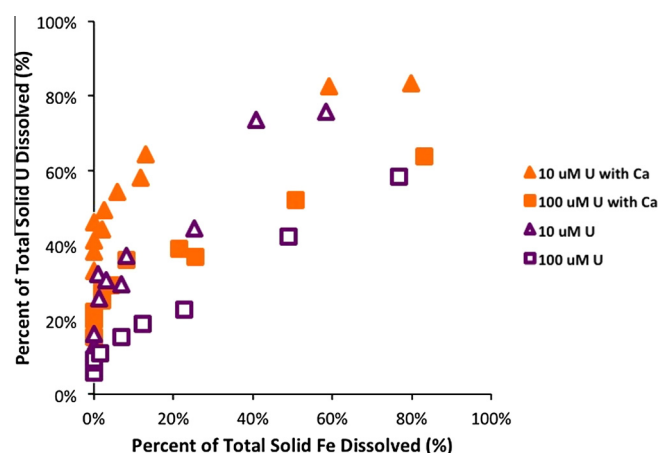


Fig. 2. Uranium and Fe release from U-bearing iron oxide solids upon reaction with 10 mM ascorbic acid at pH 3.0 for 18 days. Solids were obtained from reacting ferrihydrite with 10  $\mu\text{M}$  U and 100  $\mu\text{M}$  U, 0.3 mM Fe(II), 3.8 mM carbonate, and 0 mM Ca or 4 mM Ca, at pH 7.0.

to describe the EXAFS function for the fitting region of  $k = 3$  to  $11\text{ }\text{\AA}^{-1}$  (Fig. 4 and [Electronic Annex](#)); in all cases, the reduced chi-squared reported by Athena was  $<0.33$ , and the  $r$ -factor was  $<0.22$ . The uncertainty associated with the linear combination fitting results is  $\pm 5\text{--}15\%$  (details on uncertainty estimates are provided in the [Electronic Annex](#)).

Uranium  $L_{3\text{-edge}}$  EXAFS linear combination fits were performed to quantify the proportion of U retained in each form (adsorbed U, incorporated U, and  $UO_2$ ). Incubations with U concentrations  $\leq 10\text{ }\mu\text{M}$  had EXAFS features of adsorbed and incorporated U: 11–36% adsorbed uranyl and 64–89% incorporated U for U concentrations of 1–10  $\mu\text{M}$  in the presence and absence of Ca (Fig. 5). The range of EXAFS-derived adsorbed uranyl is consistent with the  $KHCO_3$  and ascorbic extractions for these samples (data not shown).

At  $U(VI)$  concentrations  $\geq 50\text{ }\mu\text{M}$ , the EXAFS spectra also had primarily features of adsorbed and incorporated U (Fig. 5), but all except one also included  $UO_2$  (9–32%).

All XRD patterns except for the 170  $\mu\text{M}$  U no-Ca slurry showed a low-intensity set of peaks characteristic of uraninite (Fig. 6), corroborating the EXAFS fitting results. Further, uraninite particles were observed using TEM, which occurred as  $\sim 10\text{ nm}$  domains associated with the iron oxides (Fig. 7). The EXAFS linear combination fitting shows the variation in adsorbed uranyl, incorporated U, and uraninite with changes in reaction conditions (Fig. 5). In contrast to the reactions with ferrihydrite slurry, an incubation with 0.3 mM Fe(II), 4 mM Ca, 170  $\mu\text{M}$  U, and ferrihydrite-coated sand resulted in 64% adsorbed U and 36% incorporated U (see [Electronic Annex](#)). The decreased prevalence of U incorporation in Fe-coated sand is likely attributable to the effects of dissolved/adsorbed silicate on U incorporation and iron oxide transformation (Jones et al., 2009; Boland et al., 2011). No uraninite was observed in the ferrihydrite-coated sand incubation.

Evidence of Ca–U precipitates was not observed. Digestion of solids and analysis via ICP-MS found Ca to be below detection limit ( $<0.1\text{ mg/L}$ ) in all cases. Additionally,

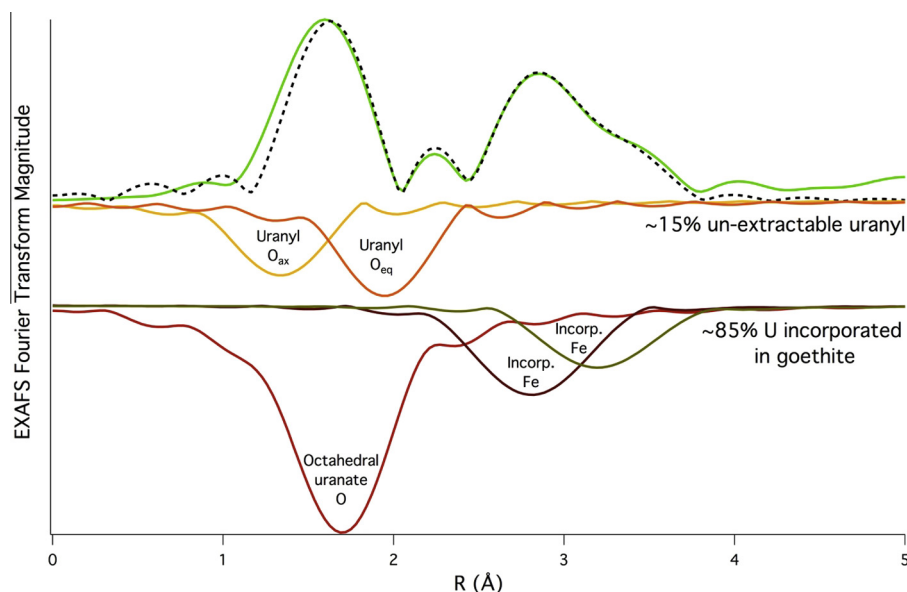


Fig. 3. Uranium L<sub>3</sub>-edge EXAFS shell-by-shell fit of incorporated U resulting from the reaction of ferrihydrite with 1  $\mu$ M U, 0.3 mM Fe(II), and 3.8 mM bicarbonate, at pH 7.0. Solids underwent bicarbonate extraction to remove adsorbed U(VI). The fits illustrate ~15% un-extracted U(VI) and ~85% U incorporated into goethite. The solid green line is the data, the dotted black line represents the overall fit, and the inverted solid lines are the individual paths (U–O and U–Fe) that make up the overall fit. (For interpretation of the references to color in this figure legend, the reader is referred to the web version of this article.)

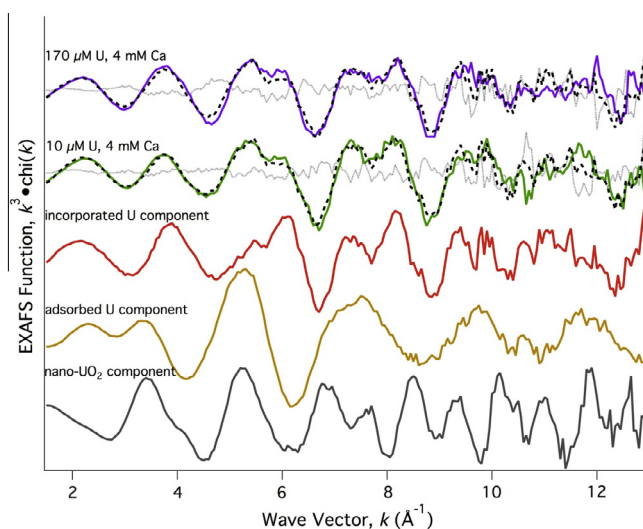


Fig. 4. EXAFS linear combination fitting results for  $k^3$ -weighted U L<sub>3</sub>-edge EXAFS spectra for ferrihydrite reacted with U(VI), 0.3 mM Fe(II), 3.8 mM carbonate, and 4 mM Ca, at pH 7.0. Data (colored lines), fitting components (incorporated U, adsorbed U, nano-UO<sub>2</sub>), linear combination fits (black dotted lines), and residuals (light grey dotted lines) are shown. (For interpretation of the references to color in this figure legend, the reader is referred to the web version of this article.)

Ca/U precipitates were not observed with TEM. Compositional analysis via EDS showed U associated with goethite and other iron oxide particles (resembling bernalite-like particles, or ferrihydrite), but no Ca was detected (data not shown). Further, Ca was not detected in XPS survey scans after the samples were rinsed with de-ionized water, further suggesting that Ca–U precipitates were either not present in this system, or were rinsed off during sample harvesting. Therefore, U in this system was determined to be

associated with iron oxide minerals (ferrihydrite, goethite, magnetite) and U minerals (UO<sub>2</sub>).

### 3.1.2. Uranium valence state

While X-ray absorption spectroscopy can readily distinguish between U(IV) and U(VI), it is less straightforward for differentiating between U(VI) and U(V) unless one has *a priori* structural models (Soldatov et al., 2007). By contrast, XPS has proven sufficient to resolve U(V) (Ilton

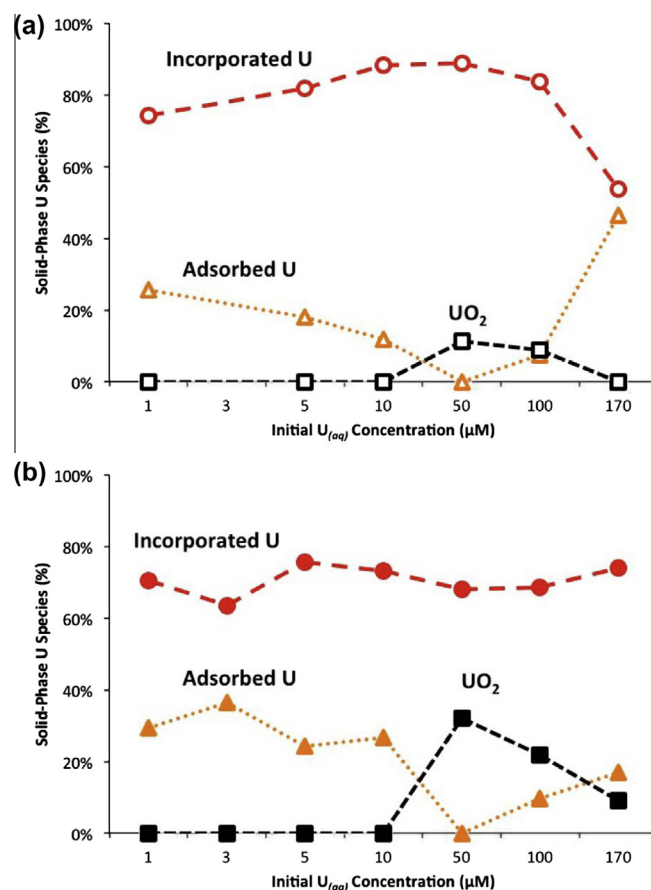


Fig. 5. Solid phase U speciation from EXAFS linear combination fits, as a function of initial U(VI)<sub>(aq)</sub> concentration ( $[U]_{\text{initial}} = 1\text{--}170\ \mu\text{M}$ ) after reaction with ferrihydrite, 0.3 mM Fe(II), 3.8 mM carbonate, and (a) 0 mM Ca, or (b) 4 mM Ca, at pH 7.0. Uranium incorporated into goethite dominates solid phase U over this range of reaction conditions. Linear combination fitting EXAFS percentages are shown for each component: incorporated U (red circles), adsorbed U (yellow triangles), and UO<sub>2</sub> (black squares). (For interpretation of the references to color in this figure legend, the reader is referred to the web version of this article.)

and Bagus, 2011; Ilton et al., 2010, 2012); we therefore utilized XPS to determine the valence state of U associated with the iron oxide reaction products. X-ray photoelectron spectroscopic analysis indicates that U(V) is the dominant oxidation state of U associated with goethite (Fig. 8). U(V) has a lower binding energy than U(VI), commonly corresponding to an approximately  $-1\ \text{eV}$  shift in the primary U4f<sub>7/2</sub> and U4f<sub>5/2</sub> peaks; however, the peak shift is supportive but not diagnostic of U(V) (Ilton and Bagus, 2011). The satellite peak structures are needed to distinguish between U(IV), U(V), and U(VI), as described by Ilton et al. (2012). Fig. 8 depicts an XPS spectrum representative of U associated with the iron oxides, which was fit with contributions from U(IV), U(V), and U(VI) at 380.4, 380.6, and 382.0 eV, respectively, for the U4f<sub>7/2</sub> peak (Table 1). The U4f<sub>7/2</sub> satellite peak at  $+8.4\ \text{eV}$  from the primary peak and the U4f<sub>5/2</sub> satellite peak at  $+8.3\ \text{eV}$  are indicative of U(V) (Fig. 8). The XPS fits also indicate the presence of both U(IV) and U(VI); satellite peaks at  $+6.8\ \text{eV}$  from the primary peaks are from U(IV), and satellite peaks at  $+3.2\ \text{eV}$  are from U(VI) (Fig. 8).

The dominant U oxidation state determined by XPS was U(V), with 56–61% as U(V) (for 10 and 100 μM U, respectively) with 0 mM Ca. With 4 mM Ca, 51% was U(V) at

both 10 and 100 μM U concentrations. Uranium(VI) was present in all samples (11–26%), as was U(IV) (22–29%). Full XPS fitting results are shown in Table 1.

### 3.1.3. Ferrihydrite transformation products

Goethite was the only observed crystalline iron oxide in the 0.3 mM Fe(II), variable-U experiments. Iron K-edge EXAFS spectroscopy indicates that approximately 30% of the post-transformation iron oxide remains as ferrihydrite and 70% is goethite (see Electronic Annex).

### 3.1.4. Amount of uranium incorporated in goethite

Direct dissolution provides a measurement of the total U:Fe ratio of the solids for the 10 μM  $[U(VI)]_{\text{initial}}$  and 100 μM  $[U(VI)]_{\text{initial}}$  systems. These can be combined with proportional estimates of incorporated U derived from EXAFS spectroscopy (Fig. 5) to establish an estimate of the amount of incorporated U. Upon acid digestion, the total U:Fe molar ratio of the 10 μM  $[U(VI)]_{\text{initial}}$  and 100 μM  $[U(VI)]_{\text{initial}}$ , 4 mM Ca systems were 0.0061 and 0.034, respectively. Combined with the EXAFS spectroscopic estimates (Fig. 5), 0.4 mol% and 2.3 mol% U were incorporated, respectively. This estimate is close to the 2–3 mol% estimate of Nico et al. (2009) for a similar system

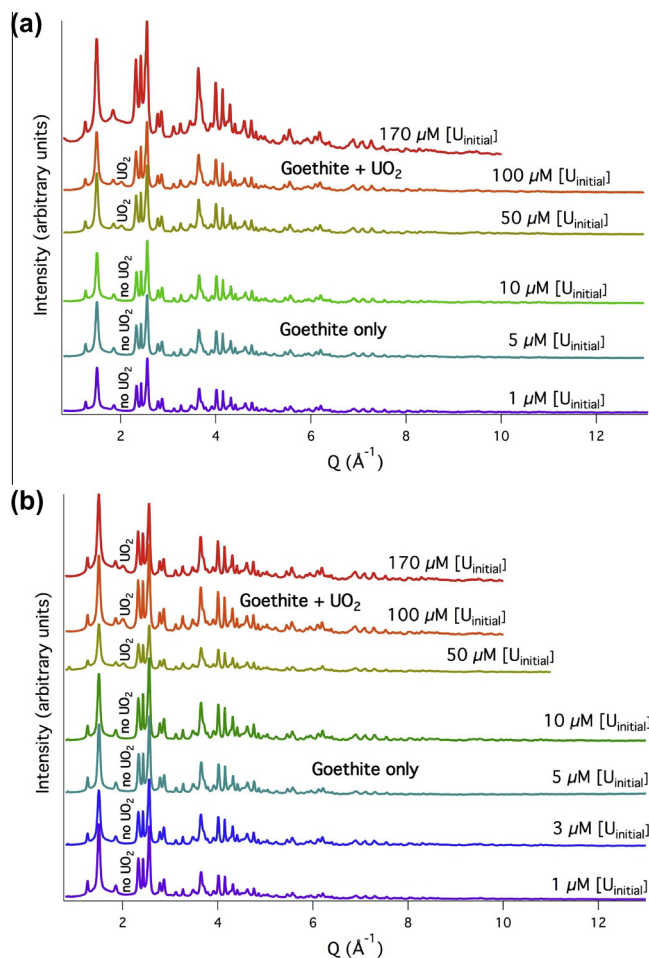


Fig. 6. Crystalline solid phases identified with high-resolution powder diffraction, resulting from U(VI) ( $[U_{\text{initial}}] = 1\text{--}170\text{ }\mu\text{M}$ ) reacted with 0.3 mM Fe(II), 3.8 mM carbonate, and (a) 0 mM Ca or (b) 4 mM Ca, at pH 7.0.

with Ca. For the system without Ca, the total U:Fe molar ratios were 0.0076 and 0.062, in the 10 and 100  $\mu\text{M}$   $[U(\text{VI})_{\text{initial}}]$ , respectively. Taking the EXAFS results into account, this corresponds to incorporated U of 0.7 mol% and 5.2 mol% in the no-Ca system.

With ferrihydrite-coated sand,  $\sim 2.3$  mol% (U:Fe) was sorbed to the solid, as measured by difference from U in solution (23% of the 170  $\mu\text{M}$  U in the system was sorbed, 77% remained in solution). Of this sorbed U, 36% ( $\sim 0.8$  mol%) was incorporated and 64% ( $\sim 1.5$  mol%) was adsorbed, an amount of U incorporation lower than that observed by Nico et al. (2009). The difference in amount of incorporation was due to the presence of ten times more Fe(II) to drive U and Fe transformations in Nico et al. (2009).

### 3.2. Variable Fe(II) incubations

Variable concentrations (0–3 mM Fe) of Fe(II) were reacted with ferrihydrite and 127  $\mu\text{M}$  uranyl at a starting pH of 7.0 (3 mM Fe) to 7.5 (0 mM Fe), with 0 mM or 4 mM Ca. Iron(II) was used to drive the reductive transformation of both ferrihydrite and U. In the absence of Ca and Fe(II), 73% of total U was adsorbed on ferrihydrite.

Addition of Fe(II) resulted in greater U removal from solution due to U incorporation into restructured iron oxides and U reduction to  $\text{UO}_2$ ; 79% of U was removed from solution at an initial Fe(II) concentration of 0.3 mM, and  $>99\%$  of U was removed from solution at Fe(II) concentrations of  $\geq 1$  mM (Fig. 9). In contrast, due to the formation of the uranyl–calcium–carbonato complex with 4 mM Ca present, only 29% of U was adsorbed when Fe(II) was absent. After Fe(II) addition, 36% of U was removed from solution at 0.3 mM Fe(II), while 85% was removed with 1 mM Fe(II), and greater than 99% of U was removed from solution at 3 mM Fe(II) concentrations (Fig. 9). Greater U removal (79–99%+) was due largely to U reduction to  $\text{UO}_2$ , especially at 3 mM Fe(II), although U incorporation in goethite, and to a lesser extent uranyl adsorption, also played a role (Fig. 10).

#### 3.2.1. Uranium solid phase speciation

At  $[Fe(\text{II})_{\text{initial}}] = 0.3$  mM, EXAFS linear combination fits showed that only 14% and 25% of solid phase U was incorporated into goethite for the 0 mM Ca and 4 mM Ca systems, respectively. The remainder of solid phase U for the lowest Fe(II) concentration was as adsorbed uranyl (Fig. 10). At higher Fe(II) concentrations (1 and 3 mM),

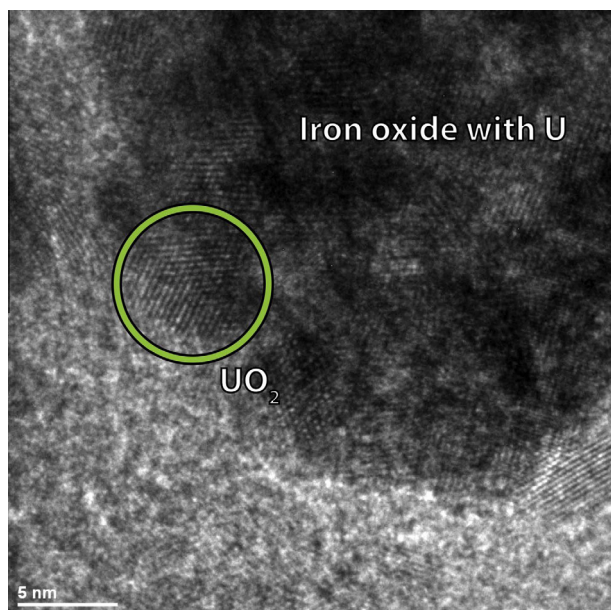


Fig. 7. Transmission electron microscope image of solids resulting from 100  $\mu\text{M}$   $[\text{U}_{\text{initial}}]$  reacted with 4 mM Ca and 0.3 mM Fe(II), at pH 7.0. Energy-dispersive X-ray spectroscopic analysis, coupled with measurements of lattice fringes for d-spacings, indicate that the particles are mixed iron oxides with U (upper right, labeled) and  $\text{UO}_2$  (center-left, circled and labeled).

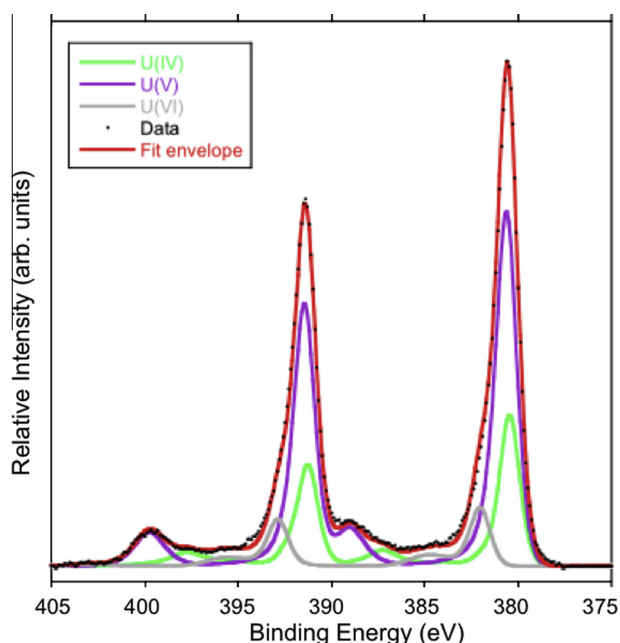


Fig. 8. X-ray photoelectron spectrum of U-bearing goethite resulting from ferrihydrite reacted with 100  $\mu\text{M}$  U and 0.3 mM Fe(II), at pH 7.0. Binding energy was referenced to adventitious C1s at 285.0 eV. The primary  $\text{U}4f_{5/2}$  peak and  $\text{U}4f_{7/2}$  peaks, along with satellite peaks, allow for quantification of U(IV) in green, U(V) in purple, and U(VI) in grey. The overall fit is shown in red. (For interpretation of the references to color in this figure legend, the reader is referred to the web version of this article.)

$\text{UO}_2$  and U(V) incorporation into goethite become prominent sinks of retained U. In the presence of 4 mM Ca, reaction of ferrihydrite with 1 mM Fe(II) resulted in 62% incorporated U, 38% as  $\text{UO}_2$ , and no remaining adsorbed uranyl (Fig. 10). At  $[\text{Fe(II)}]_{\text{initial}} = 3$  mM and with 4 mM Ca, 41% of the solid phase U was incorporated as U(V) in goethite, 41% was reduced to  $\text{UO}_2$ , and 18% remained adsorbed (Fig. 10). With no Ca, at  $[\text{Fe(II)}]_{\text{initial}} = 1$  mM, 54% of solid phase U was incorporated, 31% was reduced to  $\text{UO}_2$ , and 15% remained adsorbed. When  $[\text{Fe(II)}]_{\text{initial}}$  was increased to 3 mM with no Ca, 35% of solid phase U was incorporated, 44% was reduced to  $\text{UO}_2$ , and 21% remained adsorbed (Fig. 10). X-ray powder diffraction indicates that  $\text{UO}_2$  is present in all of the samples except those with 0.3 mM Fe(II). Samples with 1, and 3 mM Fe(II) clearly show the presence of  $\text{UO}_2$ , with both 0 and 4 mM Ca (Fig. 11). The XRD patterns corroborate the U  $L_{3\text{-edge}}$  EXAFS linear combination fitting results of 0–44%  $\text{UO}_2$ ; the  $\text{UO}_2$  is evident in the U  $L_{3\text{-edge}}$  EXAFS spectra from the 1 and 3 mM Fe(II) systems, but not the 0.3 mM Fe(II) system (Fig. 12).

Without Ca, the amount of bicarbonate extractable U varied from 45% of total U with 0 mM Fe(II) to 38% with 0.3 mM Fe(II), down to  $\sim 0\%$  for 1 mM Fe(II) and  $\sim 2\%$  for 3 mM Fe(II). The presence of Ca and the strength of the ternary uranyl–calcium–carbonate complex altered the amount of bicarbonate extractable uranyl to 16% with no Fe(II), 16% with 0.3 mM Fe(II),  $\sim 3\%$  with 1 mM Fe(II), and  $\sim 0\%$  for 3 mM Fe(II). Up to half of the adsorbed uranyl (as measured spectroscopically) was not removed by bicarbonate extraction in the 0.3 mM Fe(II) system, and almost no adsorbed uranyl was removed by bicarbonate extraction in the 1 and 3 mM Fe(II) systems.

### 3.2.2. Ferrihydrite transformation products

With an initial Fe(II) concentration of 0.3 mM, goethite with short, broad diffraction peaks was the primary observed transformation product of ferrihydrite, though the presence of Ca led to goethite with sharper diffraction peaks (Fig. 11). Substantial scattering background, presumably from residual 2-line ferrihydrite, is also present at  $[\text{Fe(II)}]_{\text{initial}} = 0.3$  mM. At an initial Fe(II) concentration of 1 mM, goethite with sharp diffraction peaks was the only iron oxide detected in the XRD analysis. At 3 mM Fe(II), magnetite was the primary Fe product, with smaller amounts of goethite (Fig. 11).

## 4. DISCUSSION

### 4.1. Competition between reaction pathways

In combination with uranyl adsorption, the fate of U within our experimental system is dependent on multiple different Fe(II)-driven processes, which all potentially occur simultaneously: U incorporation into goethite during Fe(II)-catalyzed ferrihydrite transformation to goethite, and Fe(II)-induced uranyl reduction to  $\text{UO}_2$  (Fig. 13). The fate of U in the system depends on the relative reaction rates of a suite of competing reactions. The reactions

Table 1

X-ray photoelectron spectroscopy fitting percentages for the U 4f<sub>5/2</sub> and 4f<sub>7/2</sub> primary and satellite peaks. Solids were from ferrihydrite slurry reacted with 10 μM U or 100 μM U, 0 mM Ca or 4 mM Ca, 3.8 mM carbonate, and 0.3 mM Fe(II), at pH 7.0. Uncertainty estimates are expressed as one standard deviation of replicate measurements of three separate points of XPS analysis.

U concentration (μM)	Ca concentration (mM)	U(IV), %	U(V), %	U(VI), %
10	0	21.6 ± 2.1	55.6 ± 3.6	22.8 ± 1.4
100	0	28.8 ± 0.5	60.6 ± 0.7	10.6 ± 1.1
10	4	23.0 ± 1.7	51.2 ± 1.3	25.8 ± 2.5
100	4	25.9 ± 2.1	51.1 ± 1.2	23.0 ± 2.0

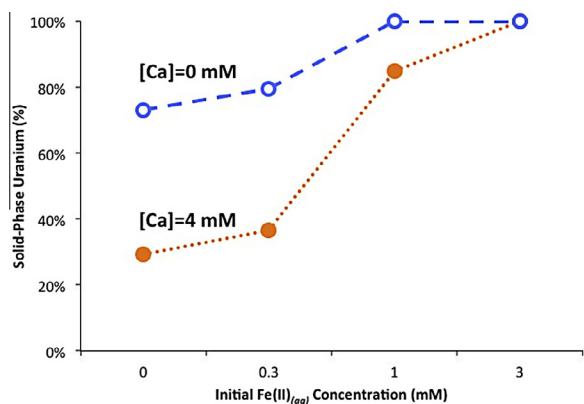
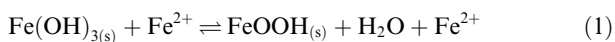


Fig. 9. Uranium partitioned into the solid phase as a function of Fe(II)<sub>(aq)</sub> concentration ([Fe(II)]<sub>initial</sub>] = 0–3 mM) and Ca<sub>(aq)</sub><sup>2+</sup> concentration (0 or 4 mM Ca) upon reaction with ferrihydrite, 127 μM U(VI), and 3.8 mM carbonate at pH 7.0–7.5. Error bars are smaller than the symbols used to represent the data and are not displayed.

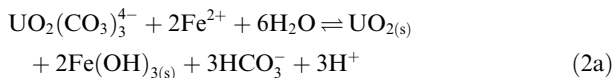
governing U fate are (all reactants/products are aqueous species unless otherwise specified):

- *Ferrihydrite transformation to goethite:*

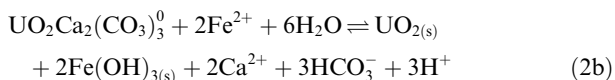


- *U(VI) reduction to UO<sub>2</sub>:*

For the uranyl–carbonato aqueous species,



For the uranyl–calcium–carbonato species,



- *U(V) incorporation, considering uranyl and uranyl–carbonato adsorption complexes:*

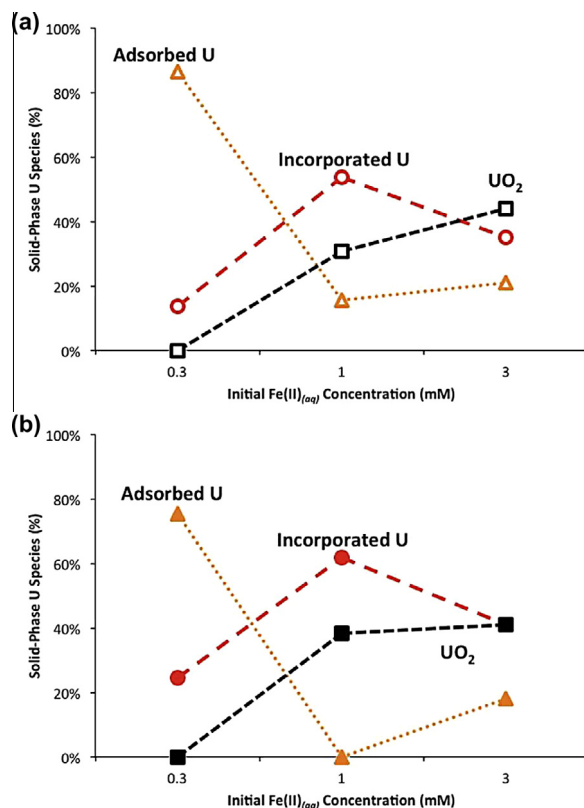
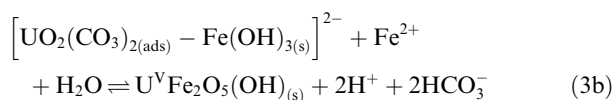
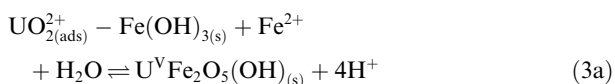


Fig. 10. Solid phase U speciation from EXAFS linear combination fits, as a function of initial Fe(II)<sub>(aq)</sub> concentration ([Fe(II)]<sub>initial</sub>] = 0.3–3 mM) after reaction with ferrihydrite, 127 μM U(VI), 3.8 mM carbonate, and (a) 0 mM Ca, or (b) 4 mM Ca, at pH 7.0–7.5. Uranium incorporated into goethite is a common form of solid phase U over this range of reaction conditions. Linear combination fitting EXAFS percentages are shown for each component: incorporated U (red circles), adsorbed U (yellow triangles), and UO<sub>2</sub> (black squares). (For interpretation of the references to color in this figure legend, the reader is referred to the web version of this article.)

Uranium incorporation into goethite is likely initiated with an adsorbed uranyl species reacting with Fe(II), as indicated in reaction 3 above. The rate of U adsorption is presumed to be rapid in comparison to reduction and incorporation, with nearly complete adsorption occurring in minutes, and equilibrium reached in hours (Giammar and Hering, 2001). The aqueous chemical factors that affect the kinetics of, and subsequent competition between, reaction pathways include: (1) Fe(II) concentration; (2) U

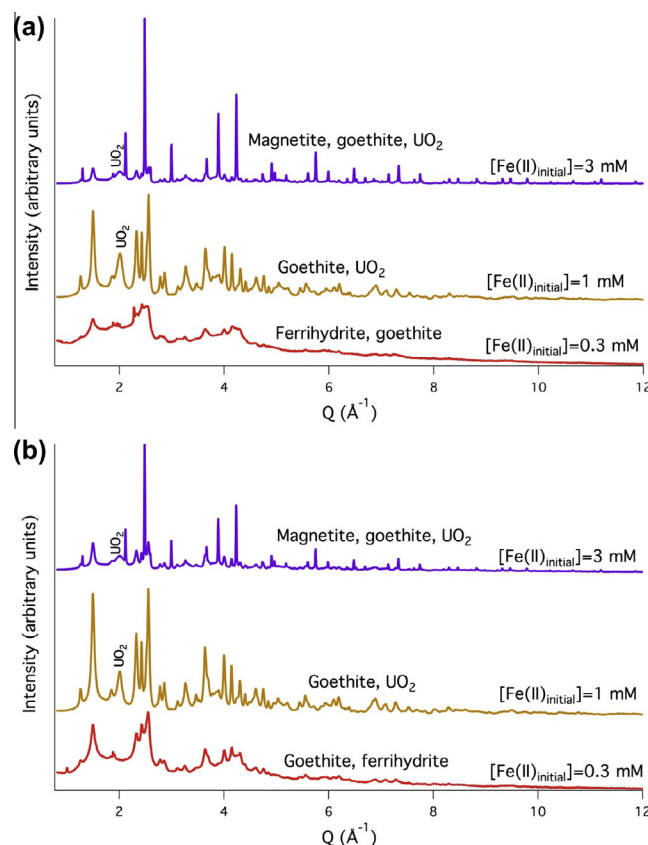


Fig. 11. Crystalline solid phases identified with high-resolution powder diffraction, resulting from Fe(II) ( $[\text{Fe(II)}]_{\text{initial}} = 0.3\text{--}3\text{ mM}$ ) reacted with  $127\text{ }\mu\text{M U(VI)}$ ,  $3.8\text{ mM carbonate}$ , and (a)  $0\text{ mM Ca}$  or (b)  $4\text{ mM Ca}$ , at pH 7.0–7.5.

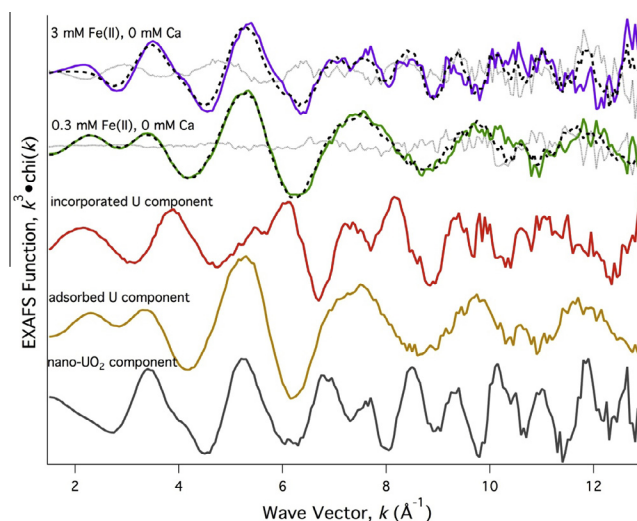


Fig. 12. EXAFS linear combination fitting results for  $k^3$ -weighted U  $L_3$ -edge EXAFS spectra for ferrihydrite reacted with  $127\text{ }\mu\text{M U(VI)}$ ,  $0.3\text{--}3\text{ mM Fe(II)}$ ,  $3.8\text{ mM carbonate}$ , and  $0\text{ mM Ca}$ , at pH 7.0–7.5. Data (colored lines), fitting components (incorporated U, adsorbed U, nano- $\text{UO}_2$ ), linear combination fits (black dotted lines), and residuals (light grey dotted lines) are shown. (For interpretation of the references to color in this figure legend, the reader is referred to the web version of this article.)

concentration; (3) pH; and (4) Ca concentration (in the presence of carbonate). The first three factors, Fe(II) and U concentrations, and pH, exert strong controls due to

their effects on iron oxide transformation and the thermodynamic favorability of U reduction. The most important parameter in determining iron oxide products and U fate

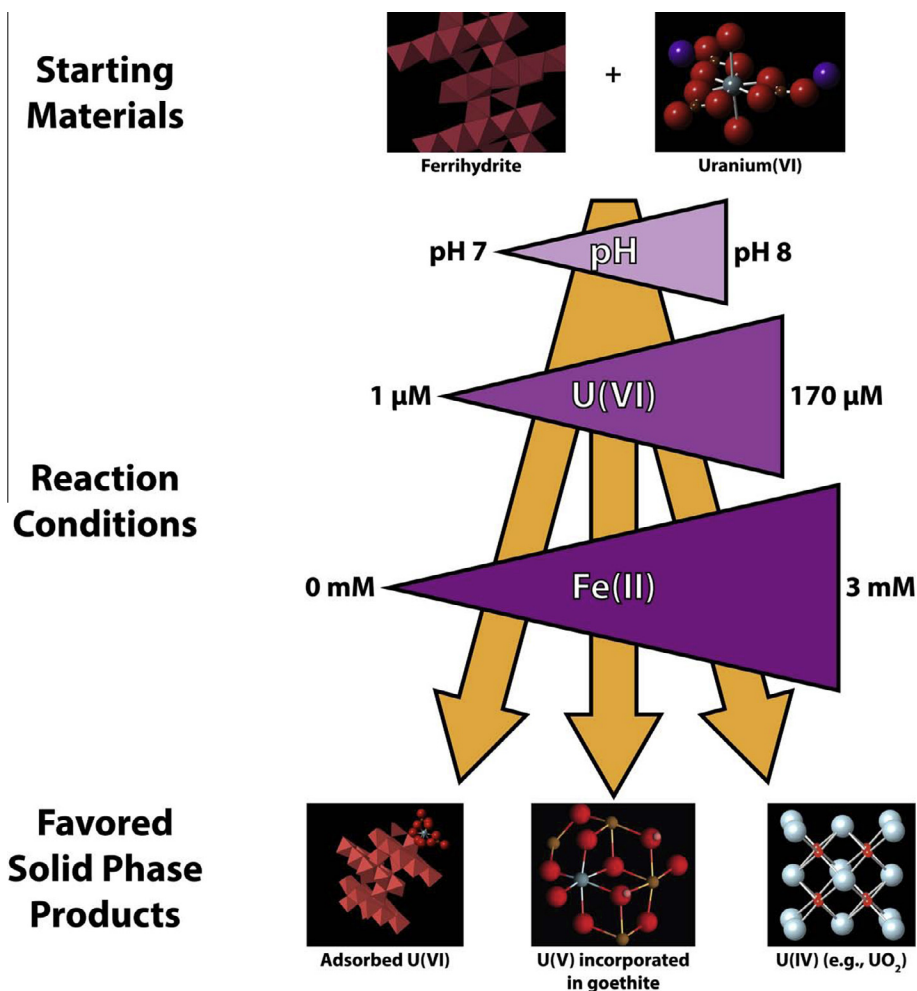


Fig. 13. Conceptual model of the predominant solid phase products (bottom) of uranyl and ferrihydrite transformation (yellow arrows). Solid phase products are influenced primarily by Fe(II) concentration, U concentration, and initial pH, with Fe(II) concentration exerting the dominant control (as indicated by the size and shading of the triangles). Higher pH, U concentration, and Fe(II) concentration favor solid phase products toward the right of the diagram (incorporated U(V) and U(IV) precipitates). (For interpretation of the references to color in this figure legend, the reader is referred to the web version of this article.)

is Fe(II) concentration, due to its central role in the three competing reactions of ferrihydrite transformation, U(VI) reduction, and U(V) incorporation. Calcium modifies these overall pathways due to its effects on uranyl aqueous speciation, with higher U concentrations favoring reduction and the presence of Ca retarding reduction.

Ferrihydrite transformation is affected by pH and Fe(II) concentration, with higher pH or Fe(II) favoring magnetite and lower pH or Fe(II) favoring goethite (Hansel et al., 2005). The pH of the system, as well as Fe(II) concentrations, can also affect iron oxide transformation kinetics. For example, Yang et al. (2010) found that Fe(II)-induced transformation of 6-line ferrihydrite to goethite and/or magnetite occurred at pH 6.8 on a timescale of days to several weeks. Boland et al. (2011) observed that 2-line ferrihydrite transformed to goethite within 4 days at pH 6.5 in the presence of 1 mM Fe(II). Hansel et al. (2005) observed the transformation of 2-line ferrihydrite ~70% goethite and ~30% ferrihydrite within 12 h at pH 7.2 upon reaction with

2 mM FeSO<sub>4</sub>, but with 0.2 mM FeSO<sub>4</sub>, the transformation to a mixture of goethite and lepidocrocite took ~40 h. Ferrihydrite transformation products and reaction kinetics are the result of an intimate interplay between Fe(II) concentrations and pH. In our system, a slight difference in initial pH led to strikingly different ferrihydrite transformation products in otherwise similar systems with 300 μM Fe(II) and 100+ μM U (e.g., Figs. 6 and 11). The inhibition of goethite formation at higher pH is consistent with previous studies (Hansel et al., 2005). The slight pH increase also produced strikingly different results with respect to U incorporation, since the decrease in goethite formation corresponded with a decrease in U incorporation (Figs. 5 and 10).

In addition to ferrihydrite transformation kinetics, U redox reaction kinetics also play a key role in the evolution of the system. The abiotic reduction of U(VI) to UO<sub>2</sub> may occur more rapidly than iron oxide transformation. Liger et al. (1999) observed the reduction of 0.5 μM U by

160  $\mu\text{M}$  Fe(II) in the presence of a hematite suspension in less than 30 h. Du et al. (2011) found that 0.21 mM U(VI) was completely reduced by 1 mM Fe(II) at pH  $\sim 8.9$  in  $\sim 20$  min, and that a pH  $\sim 6.2$  substantially slowed but did not completely inhibit U reduction. Faster  $\text{UO}_2$  precipitation relative to goethite formation led to substantially more  $\text{UO}_2$  in the 1 mM Fe(II) system (Fig. 10) versus a comparable system at a slightly lower initial pH with 300  $\mu\text{M}$  Fe(II) (Fig. 5 and 100  $\mu\text{M}$  U). The interplay between variations in reaction conditions and vastly differing reaction kinetics and products illustrates the complexity of the U/ferrihydrite/Fe(II) system.

We observed that for U concentrations ranging from 1 to 10  $\mu\text{M}$ , U incorporation into goethite is the dominant retention pathway, ranging from 64% to 89% depending on the reaction conditions (Fig. 5). Under conditions leading to Fe(II) production such as in an aquifer in low-oxygen conditions, therefore, U incorporation into goethite is likely an important and overlooked retention pathway at U concentrations  $< 10 \mu\text{M}$  (in cases where Fe(II) concentrations are on the order of hundreds of  $\mu\text{M}$ ). Boland et al. (2011) also observed U incorporation into goethite for similar conditions with one important distinction being that both calcium and carbonate were absent in their system. Given the substantial impact of carbonate and calcium on U biogeochemistry, and the ubiquity of both ions in the environment, the present findings substantiate the competitiveness of the U incorporation process in low-U systems containing carbonate and Ca.

Uranium incorporation into goethite is a dominant U retention pathway in low-U systems, and is also a competitive U retention pathway across the wide range of aqueous reaction conditions explored in this study. Incorporated U is a substantial component of the total U budget in all systems studied here (Figs. 1, 5, 9 and 10). The relative contributions of the  $\text{UO}_2$  pathway, however, increased with increasing initial aqueous U concentration, until consumption of Fe(II) limited further U reduction to U(IV). Generally, when Fe(II) concentration was not limiting, higher U concentrations accelerated U(VI) reduction to U(IV), resulting in subsequent precipitation of  $\text{UO}_2$  becoming an increasingly prominent retention pathway. Even with initial concentrations of Fe(II) as high as 3 mM, however, U incorporation into goethite remained a contributing retention pathway (Fig. 10).

#### 4.2. Effect of uranyl aqueous speciation

While the presence of calcium decreased U retention (Figs. 1 and 9) and the amount of U incorporated into iron oxide, EXAFS analysis demonstrated that U incorporation remained an operative retention process (Figs. 5 and 10). Boland et al. (2011) achieved similar EXAFS results in systems absent of carbonate, suggesting that U incorporation into ferrihydrite during Fe(II)-induced transformation does not require a particular U aqueous species. In the present study, U incorporation occurred, and was an important sequestration process, regardless of the dominant uranyl aqueous species. Incorporation occurred even though uranyl-carbonate and uranyl-calcium-carbonate complexes

decreased the extent of U adsorption (Waite et al., 1994; Stewart et al., 2010) (Figs. 1 and 9). The fraction of adsorbed uranyl, even when decreased by the uranyl-calcium-carbonate complexes, appears to provide ample precursor concentration for U incorporation.

Despite the relative lack of impact of calcium on the U incorporation process, as shown by the EXAFS linear combination fitting analysis (Figs. 5 and 10), the presence of uranyl-calcium-carbonate ternary complexes can substantially impact the fate of U by altering the mass balance (Figs. 1 and 9) and exerting a secondary influence on solid phase products. Uranyl-calcium-carbonate ternary complexation decreases the rate and extent of U(VI) reduction to U(IV) compared to Ca-free systems (Brooks et al., 2003; Hua et al., 2006; Neiss et al., 2007), and thus increased the proportion of incorporated U relative to  $\text{UO}_2$  (at  $[\text{Fe(II)}]_{\text{initial}} \geq 1 \text{ mM}$ ). Consequently, when Fe(II) is not limiting, proportionally more incorporated U occurs under conditions conducive to the formation of uranyl-calcium-carbonate ternary complexes (Fig. 10). At lower Fe(II) concentrations,  $[\text{Fe(II)}]_{\text{initial}} = 0.3 \text{ mM}$ , the presence of uranyl-calcium-carbonate ternary complexes decrease both the rates of U incorporation and U reduction to U(IV), and increase the relative rate of ferrihydrite transformation to goethite. This leads to proportionally more  $\text{UO}_2$  on the solid, since U incorporation tapers off as more goethite is formed (Fig. 5). Computations by Wander et al. (2006) suggested that reduction of uranyl-carbonate complexes occurs after Fe(II) binding to the triscarbonate complex; uranyl-calcium-carbonate ternary complexation likely slows the rate of U reduction by aqueous Fe(II) by partially blocking the binding site of Fe(II) on the uranyl ternary complex and subsequent electron transfer. A decrease in the rate of U reduction due to U ternary complexes would explain the observed differences between U reduction and U incorporation in the presence of Ca.

#### 4.3. Uranium valence state and incorporated uranium

Nico et al. (2009) and Boland et al. (2011) suggested that U incorporated in goethite might have been in the pentavalent oxidation state. Ilton et al. (2012) provided strong evidence for U(V) incorporated in the structure of hematite, and atomistic modeling by Kerisit et al. (2011) indicated that U(V) substitution for Fe(III) in goethite was a better match to the available EXAFS data than U(VI) or U(IV), assuming a deprotonation charge balance scheme. However, the U  $L_{3\text{-edge}}$  X-ray absorption edge cannot be sufficiently resolved to distinguish between U(V) and U(VI). Further, post-edge features are chiefly due to uranate coordination geometry rather than U valence state (Farges et al., 1992; Soldatov et al., 2007), and distinguishing between U(VI) and U(V) depends on qualitative comparison of these features or *a priori* structural models (e.g., Soldatov et al., 2007). Here, we used XPS to interrogate the valence state of U associated with goethite formed by reductive transformation of ferrihydrite. X-ray photoelectron spectroscopy can distinguish directly and quantitatively between U valence states using the relative energies of the  $\text{U}4f$  primary and satellite peaks (Ilton and Bagus, 2011).

X-ray photoelectron spectroscopic analysis of 10  $\mu\text{M}$  U and 100  $\mu\text{M}$  U goethite samples in the present study indicated that the dominant oxidation state is U(V) (Fig. 8). There is good agreement between EXAFS-derived and XPS-derived estimates of U(VI) and U(V), with the caveat that the surface-sensitivity of the XPS technique may underestimate U(V) if it is incorporated in the goethite structure. We do observe such an under-estimation (by  $\sim 20$ – $30\%$ ) of U(V) in the XPS measurements relative to EXAFS-derived estimates of incorporated U. Furthermore, trends in the data with increasing initial aqueous U concentration, such as an increase in surface-associated  $\text{UO}_2$  particles (i.e., U(IV) in the XPS measurements), are consistent with the conclusion that U(IV) and U(VI) are predominantly surface-associated, while U(V) is incorporated in the goethite structure itself. The assertion that U is incorporated in goethite in the pentavalent state is further supported by atomistic modeling (Kerisit et al., 2011). Incorporated U is not likely U(IV) (Kerisit et al., 2011), and the mass balance of separate measurements of U in these experiments indicates that the major component is incorporated U. Drawing on both theoretical work by Kerisit et al. (2011) and our experimental results, we conclude that incorporated U is U(V).

Therefore, since incorporated U is in the pentavalent state, electron transfer must occur from Fe(II) to U(VI), resulting in a U(V) state that is preserved within the structure of the goethite. The reduction of U to U(V) underscores the importance of redox cycling in ambient-temperature U incorporation into goethite. Indeed, without reduction of U to U(V), the transformation from uranyl coordination geometry to uranate coordination geometry may not be possible at ambient temperature on this timescale of days to weeks.

The detection of U(IV) by XPS in the 10  $\mu\text{M}$  U samples is not corroborated by the XAS or XRD data; the surface-sensitivity of XPS likely accounts for both the systematic under-estimation of U(V) (i.e., incorporated U), and the detection of U(IV), compared to EXAFS. The detection of surface-bound U(IV) in the 10  $\mu\text{M}$  U samples suggests that some U in the system may exist as surface-adsorbed, poorly-crystalline or monomeric U(IV). However, the XPS-determined U(IV) parallels the EXAFS- and TEM-detectable  $\text{UO}_2$  with increasing aqueous U concentration. This is consistent with the findings of Ilton et al. (2012), where simultaneous reduction of U(VI) in hematite and on the surface of hematite yielded U(V) and U(IV), respectively. Consequently, under reducing conditions, pentavalent U tends to be stabilized within the structures of both hematite and goethite, while U(VI) and U(IV) species may be found associated with the iron oxide surface.

#### 4.4. Mechanism of pentavalent uranium incorporation

Uranium incorporates into goethite during the Fe(II)-induced transformation of ferrihydrite under a wide variety of solution conditions. Uranium addition after ferrihydrite transformation yielded only 18% incorporated U (see [Electronic Annex](#)), likely from ferrihydrite formed after reduction of the added U(VI); this indicates the necessity

of a ferrihydrite precursor for U incorporation. We along with others (e.g., Duff et al., 2002; Smith et al., 2009) observed that co-precipitation of U and Fe during ferrihydrite synthesis by hydrolysis does not yield incorporated U. Rather, U is co-precipitated as distinct uranyl hydroxide phases or as an adsorbed phase. Heating and aging can produce uranate-coordinated U in iron oxide host phases such as hematite (Duff et al., 2002; Ilton et al., 2012), though Marshall et al. (2014) interpreted the EXAFS spectrum of U substituted for Fe(III) in hematite as uranyl with elongated axial oxygen bonds. Adsorption of U onto ferrihydrite also does not produce incorporated U in the absence of an Fe(II)- or heat-induced transformation (at least on the timescale of the present study) – although some adsorbed U can be “strongly retained/sorbed” and resistant to chemical extraction. Taken together, this evidence suggests that a redox-induced transformation of U(VI) to U(V) is necessary to induce U incorporation into goethite at ambient temperature on timescales of hours to days.

The mechanism of U incorporation into goethite occurs in four steps: (1) adsorption of the uranyl cation on the ferrihydrite surface; (2) binding and electron transfer from Fe(II) to the adsorbed uranyl cation, producing U(V) (Fig. 14); (3) a shift in U(V) to octahedral coordination (Fig. 14); and, (4) continued growth of goethite around the U(V) (Fig. 15). In the first step, uranyl adsorption occurs as a mononuclear, bidentate inner-sphere surface complex at pH 7 (Bargar et al., 1999; Rossberg et al., 2009; Hiemstra et al., 2009). In the presence of carbonate, the uranyl cation may act as a bridge between the mineral surface and the carbonate ion at circumneutral pH (Bargar et al., 1999), though there is disagreement on the nature of the surface complex in the presence of carbonate at pH < 8 (Rossberg et al., 2009). In either case, the mononuclear, bidentate inner-sphere uranyl surface complex is the likely precursor of incorporated U, and is the common link between the carbonate-free, carbonate, and calcium-carbonate systems. In the second step, Fe(II) complexes with the adsorbed uranyl complex, leading to electron transfer and creation of U(V) and Fe(III). It is also possible, but seems less likely, that Fe(II) sorbed on ferrihydrite induces electron transfer through the solid (via electron hopping) and ultimately electron donation to adsorbed U(VI). In either case, U(VI) is reduced by Fe(II) to U(V) on the ferrihydrite surface. The formation of a U(V) species appears to provide a pathway to overcome a major limitation of uranyl incorporation – a mismatch in coordination of U with that of the cation sites in the goethite (or other iron oxide) lattice. The strong trans-dioxo bonds to axial oxygen atoms within the hexavalent uranyl cation would otherwise inhibit U incorporation within the iron oxide. The axial oxygen atoms reside at a distance of  $\sim 1.8$  Å in uranyl, while measurements of incorporated U in this study and others (Nico et al., 2009; Boland et al., 2011; Ilton et al., 2012) indicate a bond distance of 2.10–2.18 Å. There are some solids, such as  $\text{RbUO}_3$  and  $\text{NaUO}_3$ , where U(V) exists in octahedral coordination with bond distances in the appropriate range (Burns, 2005; Soldatov et al., 2007). We therefore propose that electron transfer from Fe(II) induces a relaxation of the trans-dioxo bonds and an

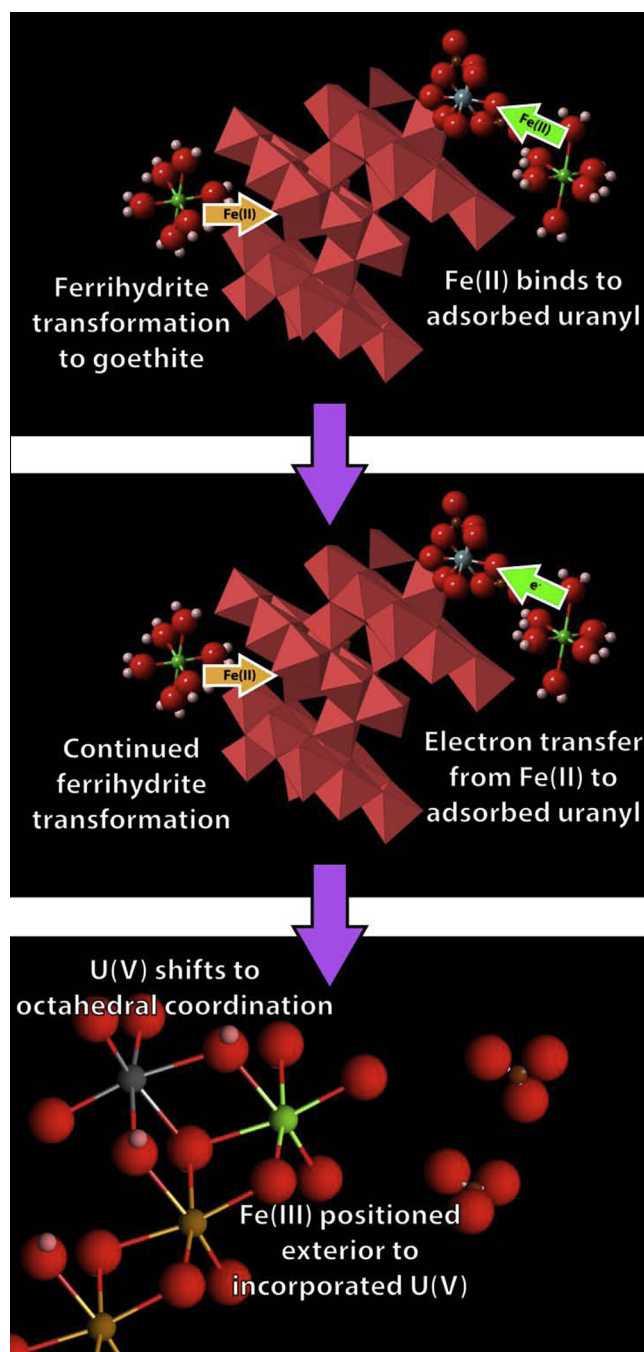


Fig. 14. Uranium incorporation mechanism. The addition of Fe(II) drives ferrihydrite transformation to goethite, and Fe(II) binding to adsorbed uranyl initiates incorporation (top). Uranium(V) incorporation occurs via electron transfer from Fe(II) to U(VI) (middle), creating a Fe(III) atom exterior to an incorporated U(V) (bottom), and enabling continued crystal growth of goethite. Uranium is grey, Fe(III) in the iron oxide is yellow, and Fe(II/III) participating in the reaction is shown in green. (For interpretation of the references to color in this figure legend, the reader is referred to the web version of this article.)

extension of the bond length between the U atom and axial O atoms from 1.80 to 2.10–2.18 Å. The electron transfer also triggers a coordination change from two axial and 5–6 equatorial O in adsorbed uranyl to octahedral coordination in the incorporated U(V)—the third step in the U incorporation mechanism (Fig. 14).

The fourth and final step in the incorporation mechanism is the formation of an Fe(III), produced by the electron transfer, that is positioned toward the exterior of the mineral relative to the newly-incorporated U(V) (Fig. 14), enabling continued crystal growth of the goethite lattice (Fig. 15). Kerisit et al. (2011) suggested that local charge

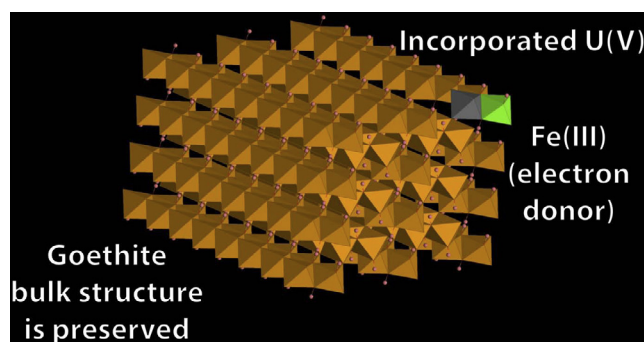
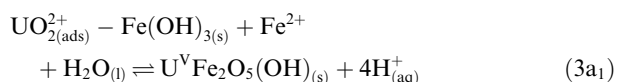


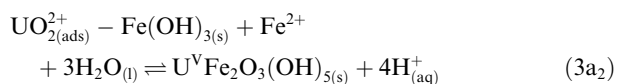
Fig. 15. The final product of the U incorporation process is a U(V) atom in octahedral coordination, with the Fe atom that was its electron donor positioned toward the exterior of the incorporated U. Local charge balance is achieved by protonation/de-protonation and/or the introduction of Fe(III) vacancies, but the bulk goethite structure is preserved. Uranium is grey, Fe(III) in the iron oxide is yellow, and Fe(II/III) participating in the reaction is shown in green. (For interpretation of the references to color in this figure legend, the reader is referred to the web version of this article.)

balance is likely achieved by the protonation or de-protonation of neighboring hydroxyl groups, with the possible formation of a vacancy at a nearby Fe(III) site. On the basis of our experimentally-determined U–O and U–Fe distances and coordination numbers (given in Table EA1) in comparison with the modeling predictions of Kerisit et al. (2011), de-protonation of hydroxyls is the most likely charge-balancing mechanism given substitution of U for Fe(III). Further, the calculated U(V)–O distances are a better match to the EXAFS data than the calculated U(VI)–O distances. The introduction of a vacancy in a neighboring Fe(III) site, and the protonation of neighboring hydroxyl, is another possible charge compensation scheme, but the bond distances, coordination numbers, and strain calculated by Kerisit et al. (2011) do not provide support for a coupled Fe(III) vacancy/protonation charge compensation scheme. However, the atomistic modeling approach is purely electrostatic, and future *ab initio* modeling may modify these conclusions.

A representative chemical reaction for Fe(II)-induced U incorporation into goethite during ferrihydrite reductive transformation is given by Eq. (3a):



Eq. (3a<sub>1</sub>) shows charge balance achieved by de-protonation only. The reaction with a Fe(III) vacancy and protonation of a hydroxyl is shown by Eq. (3a<sub>2</sub>):



As discussed above, our measurements of U oxidation state and U coordination geometry suggest that Eq. (3a<sub>1</sub>) is the likely interpretation of the U(V) incorporation mechanism (Fig. 14).

## 5. CONCLUSIONS

Other investigators (Duff et al., 2002; Ilton et al., 2012) have shown that U can be incorporated into hematite via

U/Fe co-precipitation and heating of the resulting solid material to 70 °C. We have shown that redox transformation is capable of achieving U incorporation into goethite at ambient temperatures, and that this transformation occurs within days at U and Fe(II) concentrations that are common in subsurface geochemical environments.

In the presence of ferrihydrite, with [U]<sub>initial</sub> in the range of 1–170 μM, and [Fe(II)]<sub>initial</sub> of 300 μM, U(V) incorporation was a dominant U retention pathway at pH 7.0. Redox processes including Fe(II)-induced transformation of ferrihydrite to goethite and electron transfer from Fe(II) to U(VI) are crucial to the U incorporation process. Increasing Fe(II) or U concentration, or initial pH, made U(VI) reduction to U(IV) a more competitive sequestration pathway in this system, presumably by increasing the relative rate of U reduction. Uranium concentrations commonly found in contaminated subsurface environments are often on the order of 1–10 μM (Anderson et al., 2003; Wu et al., 2006; Yabusaki et al., 2007), and groundwater Fe(II) concentrations can reach levels of 100–300 μM (Anderson et al., 2003) in reduced zones of the subsurface. Though the other necessary reactant, ferrihydrite, is often a transient solid phase in these environments, the basic geochemical conditions favoring U(V) incorporation during ferrihydrite transformation are not uncommon in natural or engineered systems. The redox-driven U(V) incorporation mechanism may help to explain U retention in some geologic materials, improving our understanding of U-based geochronology and the redox status of ancient geochemical environments. This mechanistic understanding of U incorporation may even lead to new approaches for *in situ* contamination remediation techniques, and will help refine models of U fate and transport in reduced subsurface zones.

## ACKNOWLEDGEMENTS

Support for M.M. was provided partially by the Robert and Marvel Kirby Stanford Graduate Fellowship. Additionally, this research was supported by the U.S. Department of Energy Office of Biological and Environmental Research, through the Subsurface Biogeochemical Research program (Grant number DE-SC0006772).

Funding for J.L.P. was provided by the U.S. Department of Energy Office of Biological and Environmental Research, Climate and Environmental Sciences Division, as part of the SLAC Science Focus Area Research Program (FWP #10094). E.S.I. was supported by the Geosciences Research Program in the U.S. Department of Energy, Office of Basic Energy Sciences, Division of Chemical Sciences, Geosciences & Biosciences. A portion of this research was performed using EMSL, a national scientific user facility sponsored by the U.S. Department of Energy's Office of Biological and Environmental Research and located at Pacific Northwest National Laboratory. Use of the Stanford Synchrotron Radiation Lightsource, SLAC National Accelerator Laboratory, is supported by the U.S. Department of Energy, Office of Science, Office of Basic Energy Sciences under Contract No. DE-AC02-76SF00515. The contents of this publication are solely the responsibility of the authors and do not necessarily represent the official views of NIGMS, NCRR or NIH. The authors would like to thank Moses Gonzalez and Guangchao Li for their tireless assistance. Further, the authors are indebted to Ann Marshall and Chuck Hitzman at the Stanford Nano Center for their technical expertise and patience. Additional thanks go to Peter S. Nico, and Daniel E. Giammar for their input. Three volunteer peer reviewers for GCA also provided valuable and thought-provoking feedback that substantially improved the manuscript. The authors also appreciate the technical and safety support provided by L. Amoroso, D. Day, A. Gooch, D. Menke, C. Morris, D. Murray, C. Patty, R. Russ, and the rest of the team at SSRL.

## APPENDIX A. SUPPLEMENTARY DATA

Supplementary data associated with this article can be found, in the online version, at <http://dx.doi.org/10.1016/j.gca.2014.07.016>.

## REFERENCES

- Allard T., Ildefonse P., Beaucaire C. and Calas G. (1999) Structural chemistry of uranium associated with Si, Al, Fe gels in a granitic uranium mine. *Chem. Geol.* **158**, 81–103.
- Anderson R., Vronis H., Ortiz-Bernad I., Resch C., Long P., Dayvault R., Karp K., Marutzky S., Metzler D., Peacock A., White D., Lowe M. and Lovley D. (2003) Stimulating the in situ activity of Geobacter species to remove uranium from the groundwater of a uranium-contaminated aquifer. *Appl. Environ. Microbiol.* **69**, 5884–5891.
- Ankudinov A. L., Rehr J. J. and Conradson S. D. (1998) Real-space multiple-scattering calculation and interpretation of X-ray-absorption near-edge structure. *Phys. Rev. B* **58**, 7565–7576.
- Bargar J., Reitmeier R. and Davis J. (1999) Spectroscopic confirmation of uranium(VI)-carbonate adsorption complexes on hematite. *Environ. Sci. Technol.* **33**, 2481–2484.
- Bernier-Latmani R., Veeramani H., Vecchia E. D., Junier P., Lezama-Pacheco J. S., Suvorova E. I., Sharp J. O., Wigginton N. S. and Bargar J. R. (2010) Non-uraninite products of microbial U(VI) reduction. *Environ. Sci. Technol.* **44**, 9456–9462.
- Boland D. D., Collins R. N., Payne T. E. and Waite T. D. (2011) Effect of amorphous Fe(III) oxide transformation on the Fe(II)-mediated reduction of U(VI). *Environ. Sci. Technol.* **45**, 1327–1333.
- Boyanov M. I., O'Loughlin E. J., Roden E. E., Fein J. B. and Kemner K. M. (2007) Adsorption of Fe(II) and U(VI) to carboxyl-functionalized microspheres: the influence of speciation on uranyl reduction studied by titration and XAFS. *Geochim. Cosmochim. Acta* **71**, 1898–1912.
- Boyanov M. I., Fletcher K. E., Kwon M. J., Rui X., O'Loughlin E. J., Löffler F. E. and Kemner K. M. (2011) Solution and microbial controls on the formation of reduced U(IV) species. *Environ. Sci. Technol.* **45**, 8336–8344.
- Brooks S. C., Taylor D. L. and Jardine P. M. (1996) Reactive transport of EDTA-complexed cobalt in the presence of ferrihydrite. *Geochim. Cosmochim. Acta* **60**, 1899–1908.
- Brooks S., Fredrickson J., Carroll S., Kennedy D., Zachara J., Plymale A., Kelly S., Kemner K. and Fendorf S. (2003) Inhibition of bacterial U(VI) reduction by calcium. *Environ. Sci. Technol.* **37**, 1850–1858.
- Burns P. (2005) U<sup>6+</sup> Minerals and inorganic compounds: insights into an expanded structural hierarchy of crystal structures. *Can. Mineral.* **43**, 1839–1894.
- Burns P. C. and Finch R. J. (1999) Wyartite: crystallographic evidence for the first pentavalent-uranium mineral. *Am. Mineral.* **84**, 1456–1460.
- Catalano J. G. and Brown G. E. (2004) Analysis of uranyl-bearing phases by EXAFS spectroscopy: interferences, multiple scattering, accuracy of structural parameters, and spectral differences. *Am. Mineral.* **89**, 1004–1021.
- Catalano J., Heald S., Zachara J. and Brown G. (2004) Spectroscopic and diffraction study of uranium speciation in contaminated vadose zone sediments from the Hanford Site, Washington State. *Environ. Sci. Technol.* **38**, 2822–2828.
- Chakraborty S., Favre F., Banerjee D., Scheinost A. C., Mullet M., Ehrhardt J.-J., Brendle J., Vidal L. and Charlet L. (2010) U(VI) Sorption and reduction by Fe(II) sorbed on montmorillonite. *Environ. Sci. Technol.* **44**, 3779–3785.
- DOE (1997) *Linking Legacies: Connecting the Cold War Nuclear Weapons Production Processes to Their Environmental Consequences*. US Department of Energy.
- Du X., Boonchayaanant B., Wu W.-M., Fendorf S., Bargar J. and Criddle C. S. (2011) Reduction of uranium(VI) by soluble iron(II) conforms with thermodynamic predictions. *Environ. Sci. Technol.* **45**, 4718–4725.
- Duff M., Coughlin J. and Hunter D. (2002) Uranium co-precipitation with iron oxide minerals. *Geochim. Cosmochim. Acta* **66**, 3533–3547.
- Farges F., Ponader C. W., Calas G. and Brown, Jr., G. E. (1992) Structural environments of incompatible elements in silicate glass/melt systems: II. U(IV), U(V), and U(VI). *Geochim. Cosmochim. Acta* **56**, 4205–4220.
- Finch R. and Murakami T. (1999) Systematics and paragenesis of uranium minerals. *Rev. Mineral. Geochem.* **38**, 91–179.
- Giammar D. and Hering J. (2001) Time scales for sorption-desorption and surface precipitation of uranyl on goethite. *Environ. Sci. Technol.* **35**, 3332–3337.
- Gómez P., Garralón A., Buil B., Turrero M. J., Sánchez L. and la Cruz de B. (2006) Modeling of geochemical processes related to uranium mobilization in the groundwater of a uranium mine. *Sci. Total Environ.* **366**, 295–309.
- Gu B., Brooks S. C., Roh Y. and Jardine P. M. (2003) Geochemical reactions and dynamics during titration of a contaminated groundwater with high uranium, aluminum, and calcium. *Geochim. Cosmochim. Acta* **67**, 2749–2761.
- Hansel C., Benner S., Neiss J., Dohnalkova A., Kukkadapu R. and Fendorf S. (2003) Secondary mineralization pathways induced by dissimilatory iron reduction of ferrihydrite under advective flow. *Geochim. Cosmochim. Acta* **67**, 2977–2992.
- Hansel C. M., Benner S. G. and Fendorf S. (2005) Competing Fe(II)-induced mineralization pathways of ferrihydrite. *Environ. Sci. Technol.* **39**, 7147–7153.

- Herbel M. and Fendorf S. (2006) Biogeochemical processes controlling the speciation and transport of arsenic within iron coated sands. *Chem. Geol.* **228**, 16–32.
- Hiemstra T., Van Riemsdijk W. H., Rossberg A. and Ulrich K.-U. (2009) A surface structural model for ferrihydrite II: adsorption of uranyl and carbonate. *Geochim. Cosmochim. Acta* **73**, 4437–4451.
- Hua B. and Deng B. (2008) Reductive immobilization of uranium(VI) by amorphous iron sulfide. *Environ. Sci. Technol.* **42**, 8703–8708.
- Hua B., Xu H., Terry J. and Deng B. (2006) Kinetics of uranium(VI) reduction by hydrogen sulfide in anoxic aqueous systems. *Environ. Sci. Technol.* **40**, 4666–4671.
- Hyun S. P., Davis J. A., Sun K. and Hayes K. F. (2012) Uranium(VI) reduction by iron(II) monosulfide mackinawite. *Environ. Sci. Technol.* **46**, 3369–3376.
- IAEA (2004) *The Long Term Stabilization of Uranium Mill Tailings*. International Atomic Energy Agency.
- Ilton E. S. and Bagus P. S. (2011) XPS determination of uranium oxidation states. *Surf. Interface Anal.* **43**, 1549–1560.
- Ilton E. S., Haiduc A., Cahill C. L. and Felmy A. R. (2005) Mica surfaces stabilize pentavalent uranium. *Inorg. Chem.* **44**, 2986–2988.
- Ilton E. S., Boily J.-F., Buck E. C., Skomurski F. N., Rosso K. M., Cahill C. L., Bargar J. R. and Felmy A. R. (2010) Influence of dynamical conditions on the reduction of U(VI) at the magnetite–solution interface. *Environ. Sci. Technol.* **44**, 170–176.
- Ilton E. S., Pacheco J. S. L., Bargar J. R., Shi Z., Liu J., Kovarik L., Engelhard M. H. and Felmy A. R. (2012) Reduction of U(VI) incorporated in the structure of hematite. *Environ. Sci. Technol.* **46**, 9428–9436.
- Jones A. M., Collins R. N., Rose J. and Waite T. D. (2009) The effect of silica and natural organic matter on the Fe(II)-catalysed transformation and reactivity of Fe(III) minerals. *Geochim. Cosmochim. Acta* **73**, 4409–4422.
- Kerisit S., Felmy A. R. and Ilton E. S. (2011) Atomistic simulations of uranium incorporation into iron (hydr)oxides. *Environ. Sci. Technol.* **45**, 2770–2776.
- Larsen O. and Postma D. (2001) Kinetics of reductive bulk dissolution of lepidocrocite, ferrihydrite, and goethite. *Geochim. Cosmochim. Acta* **65**, 1367–1379.
- Larson A. C. and Von Dreele R. B. (2000) *GSAS*. Los Alamos National Laboratory.
- Latta D. E., Boyanov M. I., Kemner K. M., O'Loughlin E. J. and Scherer M. M. (2012a) Abiotic reduction of uranium by Fe(II) in soil. *Appl. Geochem.* **27**, 1512–1524.
- Latta D. E., Gorski C. A., Boyanov M. I., O'Loughlin E. J., Kemner K. M. and Scherer M. M. (2012b) Influence of magnetite stoichiometry on UVI reduction. *Environ. Sci. Technol.* **46**, 778–786.
- Liger E., Charlet L. and Van Cappellen P. (1999) Surface catalysis of uranium(VI) reduction by iron(II). *Geochim. Cosmochim. Acta* **63**, 2939–2955.
- Lovley D. R. and Phillips E. J. (1992a) Reduction of uranium by *Desulfovibrio desulfuricans*. *Appl. Environ. Microbiol.* **58**, 850–856.
- Lovley D. R. and Phillips E. J. P. (1992b) Bioremediation of uranium contamination with enzymatic uranium reduction. *Environ. Sci. Technol.* **26**, 2228–2234.
- Marshall T. A., Morris K., Law G. T. W., Livens F. R., Mosselmans J. F. W., Bots P. and Shaw S. (2014) Incorporation of uranium into hematite during crystallization from ferrihydrite. *Environ. Sci. Technol.* **48**, 3724–3731.
- Neiss J., Stewart B. D., Nico P. S. and Fendorf S. (2007) Speciation-dependent microbial reduction of uranium within iron-coated sands. *Environ. Sci. Technol.* **41**, 7343–7348.
- Nico P. S., Stewart B. D. and Fendorf S. (2009) Incorporation of oxidized uranium into Fe (hydr)oxides during Fe(II) catalyzed remineralization. *Environ. Sci. Technol.* **43**, 7391–7396.
- Payne T. E. and Airey P. L. (2006) Radionuclide migration at the Koongarra uranium deposit, Northern Australia – lessons from the Alligator Rivers analogue project. *Phys. Chem. Earth A/B/C* **31**, 572–586.
- Payne T. E., Davis J. A. and Waite T. D. (1994) Uranium retention by weathered schists-the role of iron minerals. *Radiochim. Acta* **66**, 297–303.
- Pett-Ridge J. C., Monastera V. M., Derry L. A. and Chadwick O. A. (2007) Importance of atmospheric inputs and Fe-oxides in controlling soil uranium budgets and behavior along a Hawaiian chronosequence. *Chem. Geol.* **244**, 691–707.
- Postma D. (1993) The reactivity of iron oxides in sediments: a kinetic approach. *Geochim. Cosmochim. Acta* **57**, 5027–5034.
- Ravel B. (2001) ATOMS: crystallography for the X-ray absorption spectroscopist. *J. Synchrotron Radiat.* **8**, 314–316.
- Ravel B. and Newville M. (2005) ATHENA, ARTEMIS, HEPHAESTUS: data analysis for X-ray absorption spectroscopy using IFEFFIT. *J. Synchrotron Radiat.* **12**, 537–541.
- Riley R. and Zachara J. (1992) *Chemical Contaminants on Doe Lands and Selection of Contaminant Mixtures for Subsurface Science Research*. US Department of Energy, Washington, D.C. 77p. (report number DOE/ER-0547T).
- Rossberg A., Ulrich K.-U., Weiss S., Tsushima S., Hiemstra T. and Scheinost A. C. (2009) Identification of uranyl surface complexes on ferrihydrite: advanced EXAFS data analysis and CD-MUSIC modeling. *Environ. Sci. Technol.* **43**, 1400–1406.
- Sato T., Murakami T., Yanase N., Isobe H., Payne T. E. and Airey P. L. (1997) Iron nodules scavenging uranium from groundwater. *Environ. Sci. Technol.* **31**, 2854–2858.
- Senko J. M., Suflita J. M. and Krumholz L. R. (2005) Geochemical controls on microbial nitrate-dependent U(IV) oxidation. *Geomicrobiol. J.* **22**, 371–378.
- Sheng L., Szymanowski J. and Fein J. B. (2011) The effects of uranium speciation on the rate of U(VI) reduction by *Shewanella oneidensis* MR-1. *Geochim. Cosmochim. Acta* **75**, 3558–3567.
- Singer D. M., Chatman S. M., Ilton E. S., Rosso K. M., Banfield J. F. and Waychunas G. A. (2012) U(VI) Sorption and reduction kinetics on the magnetite (111) surface. *Environ. Sci. Technol.* **46**, 3821–3830.
- Skomurski F. N., Ilton E. S., Engelhard M. H., Arey B. W. and Rosso K. M. (2011) Heterogeneous reduction of U<sup>6+</sup> by structural Fe<sup>2+</sup> from theory and experiment. *Geochim. Cosmochim. Acta* **75**, 7277–7290.
- Smith S. C., Douglas M., Moore D. A., Kukkadapu R. K. and Arey B. W. (2009) Uranium extraction from laboratory-synthesized, uranium-doped hydrous ferric oxides. *Environ. Sci. Technol.* **43**, 2341–2347.
- Soderholm L., Skanthakumar S., Gorman-Lewis D., Jensen M. P. and Nagy K. L. (2008) Characterizing solution and solid-phase amorphous uranyl silicates. *Geochim. Cosmochim. Acta* **72**, 140–150.
- Soldatov A. V., Lamoén D., Konstantinović M. J., Van den Berghe S., Scheinost A. C. and Verwerf M. (2007) Local structure and oxidation state of uranium in some ternary oxides: X-ray absorption analysis. *J. Solid State Chem.* **180**, 54–61.
- Stewart B., Neiss J. and Fendorf S. (2007) Quantifying constraints imposed by calcium and iron on bacterial reduction of uranium(VI). *J. Environ. Qual.* **36**, 363–372.

- Stewart B. D., Nico P. S. and Fendorf S. (2009) Stability of uranium incorporated into Fe (hydr)oxides under fluctuating redox conditions. *Environ. Sci. Technol.* **43**, 4922–4927.
- Stewart B. D., Mayes M. A. and Fendorf S. (2010) Impact of uranyl–calcium–carbonato complexes on uranium(VI) adsorption to synthetic and natural sediments. *Environ. Sci. Technol.* **44**, 928–934.
- Stookey L. (1970) Ferrozine – a new spectrophotometric reagent for iron. *Anal. Chem.* **42**, 779–781.
- Stubbs J. E., Elbert D. C., Veblen D. R. and Zhu C. (2006) Electron microbeam investigation of uranium-contaminated soils from Oak Ridge, TN, USA. *Environ. Sci. Technol.* **40**, 2108–2113.
- Stubbs J. E., Veblen L. A., Elbert D. C., Zachara J. M., Davis J. A. and Veblen D. R. (2009) Newly recognized hosts for uranium in the Hanford Site vadose zone. *Geochim. Cosmochim. Acta* **73**, 1563–1576.
- Suzuki Y., Kelly S., Kemner K. and Banfield J. (2002) Radionuclide contamination – nanometre-size products of uranium bioreduction. *Nature* **419**, 134–134.
- Toby B. (2001) EXPGUI, a graphical user interface for GSAS. *J. Appl. Crystallogr.* **34**, 210–213.
- Waite T. D., Davis J. A., Payne T. E., Waychunas G. A. and Xu N. (1994) Uranium(VI) adsorption to ferrihydrite: application of a surface complexation model. *Geochim. Cosmochim. Acta* **58**, 5465–5478.
- Wander M. C. F. and Shuford K. L. (2012) A theoretical study of the qualitative reaction mechanism for the homogeneous disproportionation of pentavalent uranyl ions. *Geochim. Cosmochim. Acta* **84**, 177–185.
- Wander M. C. F., Kerisit S., Rosso K. M. and Schoonen M. A. A. (2006) Kinetics of triscarbonato uranyl reduction by aqueous ferrous iron: a theoretical study. *J. Phys. Chem. A* **110**, 9691–9701.
- Wang Z., Zachara J. M., Gassman P. L., Liu C., Qafoku O., Yantasee W. and Catalano J. G. (2005) Fluorescence spectroscopy of U(VI)-silicates and U(VI)-contaminated Hanford sediment. *Geochim. Cosmochim. Acta* **69**, 1391–1403.
- Webb S. M. (2005) SIXPack a graphical user interface for XAS analysis using IFEFFIT. *Phys. Scr.*, 1011.
- Wilkins M. J., Livens F. R., Vaughan D. J. and Lloyd J. R. (2006) The impact of Fe(III)-reducing bacteria on uranium mobility. *Biogeochemistry* **78**, 125–150.
- Wu W.-M., Carley J., Gentry T., Ginder-Vogel M., Fienen M., Mehlhorn T., Yan H., Carroll S., Pace M., Nyman J., Luo J., Gentile M., Fields M., Hickey R., Gu B., Watson D., Cirpka O., Zhou J., Fendorf S., Kitanidis P., Jardine P. and Criddle C. (2006) Pilot-scale in situ bioremediation of uranium in a highly contaminated aquifer. 2. Reduction of U(VI) and geochemical control of U(VI) bioavailability. *Environ. Sci. Technol.* **40**, 3986–3995.
- Yabusaki S. B., Fang Y., Long P. E., Resch C. T., Peacock A. D., Komlos J., Jaffe P. R., Morrison S. J., Dayvault R. D., White D. C. and Anderson R. T. (2007) Uranium removal from groundwater via in situ biostimulation: field-scale modeling of transport and biological processes. *J. Contam. Hydrol.* **93**, 216–235.
- Yang L., Steefel C. I., Marcus M. A. and Bargar J. R. (2010) Kinetics of Fe(II)-catalyzed transformation of 6-line ferrihydrite under anaerobic flow conditions. *Environ. Sci. Technol.* **44**, 5469–5475.

Associate editor: Marc Norman